JGR Planets

RESEARCH ARTICLE
10.1029/2023JE007963

Spectral Analysis of Mare Ingenii Basin (Lunar Farside)

Giulia Salari[1], Gloria Tognon[2], Francesca Zambon[1], Cristian Carli[1], Federico Tosi[1], Lorenza Giacomini[1], Jean-Philippe Combe[3], Riccardo Pozzobon[4], Sergio Fonte[1], Matteo Massironi[2,4], and Giovanna Rinaldi[1]

[1]Istituto Nazionale di Astrofisica – Istituto di Astrofisica e Planetologia Spaziali (INAF-IAPS), Rome, Italy, [2]Centro di Ateneo di Studi e Attività Spaziali (CISAS), Università degli Studi di Padova, Padova, Italy, [3]Planetary Science Institute (PSI), Tucson, AZ, USA, [4]Dipartimento di Geoscienze, Università degli Studi di Padova, Padova, Italy

Abstract Mare Ingenii is a site of great interest for lunar geology as it is one of the few basaltic plains on the farside of the Moon. It is located within the outer edge of the South Pole-Aitken basin, the largest and oldest impact basin in our Solar System. Mare Ingenii includes two large craters, Thomson and Thomson M, and a prominent swirl, a high-albedo sinuous feature whose origin is still debated. We conducted spectral analysis on 28 selected regions of interest within Mare Ingenii, with the aim of inferring its mineralogy. We considered reflectance data acquired in the visible to near-infrared spectral range by the Moon Mineralogy Mapper (M^3) imaging spectrometer onboard the Chandrayaan-1 mission, to derive a set of spectral parameters. Our results show wide compositional variability, with the dark material of the mare basaltic floor showing the centers of the Fe^{2+} absorption bands of the pyroxenes shifted toward long wavelengths (0.96–0.99 and 2.03–2.12 μm, respectively), consistent with the spectral characteristics of high-Ca pyroxenes (as well as swirl material and intermediate albedo regions). In contrast, the bright material of the small surrounding craters shows Fe^{2+} absorption bands shifted toward short wavelengths (0.91–0.94 and 1.91–2.04 μm, respectively), more consistent with low-Ca or Ca-free pyroxenes. The obtained results suggest a mafic signature throughout the surface of Mare Ingenii, probably representative of the composition of the lower lunar crust.

Plain Language Summary Mare Ingenii is one of the few basaltic plains on the farside of the Moon within the South Pole-Aitken basin, the oldest and largest impact basin in our Solar System. It includes two large craters, Thomson and Thomson M, and a swirl. We selected 28 regions of interest within Mare Ingenii and examined reflectance data acquired in the visible to near-infrared spectral range by the Moon Mineralogy Mapper (M^3) imaging spectrometer onboard the Chandrayaan-1 mission, with the aim of studying its mineralogy using several spectral parameters. The dark basaltic plain material, swirl and intermediate reflectance regions, show absorption bands consistent with high-calcium pyroxenes. In contrast, the bright material of the small surrounding craters shows spectral characteristics suggestive of low-calcium or calcium-free pyroxenes. The surface of Mare Ingenii is overall rich in iron and likely representative of the composition of the Moon's lower crust.

Key Points:

- Mare Ingenii is one of the few basaltic maria occurring on the lunar farside, important target also for its pit and its swirl morphology
- Analysis of spectral parameters from Chandrayaan-1/M^3 data reveals a variability in the Ingenii basin, mostly dominated by pyroxenes
- Mare Ingenii shows compositions likely representing mare deposits encompassed in a regional setting of the deeper lunar primordial crust

Correspondence to:
G. Salari,
giulia.salari@inaf.it

Citation:
Salari, G., Tognon, G., Zambon, F., Carli, C., Tosi, F., Giacomini, L., et al. (2023). Spectral analysis of Mare Ingenii basin (lunar farside). *Journal of Geophysical Research: Planets*, *128*, e2023JE007963. https://doi.org/10.1029/2023JE007963

Received 21 JUN 2023
Accepted 27 NOV 2023

Author Contributions:
Conceptualization: Giulia Salari, Francesca Zambon, Federico Tosi
Data curation: Francesca Zambon, Sergio Fonte
Formal analysis: Giulia Salari, Gloria Tognon, Francesca Zambon, Jean-Philippe Combe
Funding acquisition: Federico Tosi
Investigation: Giulia Salari, Gloria Tognon, Francesca Zambon, Cristian Carli, Federico Tosi, Jean-Philippe Combe
Methodology: Giulia Salari, Gloria Tognon, Francesca Zambon
Project Administration: Federico Tosi
Software: Francesca Zambon
Supervision: Giulia Salari, Federico Tosi
Validation: Federico Tosi
Visualization: Gloria Tognon, Lorenza Giacomini

1. Introduction

The Moon is the Earth's unique natural satellite and still preserves the record of its geological evolution. Unlike the Earth, it has no active plate tectonics. As such, unraveling the processes occurring on its surface can be the key for understanding insights on its magmatic and thermal evolution, as well as on the early stages of the Solar System. Indeed, visible to near-infrared spectroscopy is a powerful approach for mapping mineralogical phases on planetary surfaces and it is always considered for investigating other planetary bodies in our Solar System.

On the Moon, mare regions and basaltic volcanism are restricted to few limited areas on the farside, different from the nearside which appears dominated by mare deposits and dark basaltic infills. Indeed, huge lava covering is almost entirely lacking on the farside which instead appears to be heavily cratered and more homogeneous. This dichotomy is one of the most distinctive features of the Moon and still represents a very debated issue (Farcy et al., 2021; Garrick-Bethell et al., 2010; Jutzi & Asphaug, 2011; Ohtake et al., 2012; Roy et al., 2014; Zhu et al., 2019). The farside has always been studied via orbiting spacecraft and little is known about its compositions, although some estimates of its bulk chemistry and rock minerals have been made by lunar meteorites (Gross et al., 2020; Korotev et al., 2003; Nagaoka et al., 2013; Shearer et al., 2015).

Writing – original draft: Giulia Salari, Gloria Tognon
Writing – review & editing: Gloria Tognon, Francesca Zambon, Cristian Carli, Federico Tosi, Lorenza Giacomini, Jean-Philippe Combe, Riccardo Pozzobon, Sergio Fonte, Matteo Massironi, Giovanna Rinaldi

Mare Ingenii is one of the few basaltic maria occurring on the lunar farside (along with Mare Moscoviense and Mare Orientale, Karthi et al., 2022), making this still unexplored area an important target region for a better understanding of the surface compositions of the Moon.

The Ingenii basin is a ∼315 km diameter impact structure situated on the lunar farside (33.25°S, 164.83°E; Figure 1). It is located in the north-western outer part of the Pre-Nectarian (i.e., > 3.9 Ga; Wilhelms et al., 1987) South Pole-Aitken (SPA) basin, the largest (∼2,500 km in diameter) and deepest (∼13 km lower than the surrounding highlands, Spudis et al., 1994) impact basin on the Moon and in our Solar System. The Ingenii basin was largely modified by two younger craters, renamed Thomson (∼120 km in diameter) and Thomson M (∼100 km in diameter), lying on its south-eastern portion. These craters were very likely responsible for the formation of the basaltic mare covering the basin (Kramer et al., 2011b). One of most relevant discoveries occurring inside Thomson M crater, was a ∼130 m diameter irregularly shaped hole, known as pit, likely generated by the collapse of a lava tube's roof (Haruyama et al., 2009, 2010) and which shows a look at the different layers of basalts and regolith constituting the mare floor. The pits are important lunar targets, as they might represent natural shelters against the space environment, then offering potential locations for future lunar bases. Yet, another important feature of Mare Ingenii is its lunar swirl. Swirls are defined as high-albedo surface features with twisted shapes whose origins are still to be fully investigated (Hood et al., 2001) and notably their occurrence seems to be limited to the lunar surface.

These features are thought to be likely correlated to crustal magnetic anomalies (Garrick-Bethell et al., 2011; Hood et al., 2001; Pinet et al., 2000), which seem to be mostly restricted to the NW margin of the SPA basin. An extensive characterization of this area and a better understanding of swirl formation can be useful to reveal information about the magnetic history of the Moon. Moreover, the large structure of the SPA basin represents an important key target as it is the Moon's oldest and deepest (>12 km, Smith et al., 2010) impact basin (Wilhelms et al., 1979) and its composition is unusually enriched in iron-bearing materials (X. Zhang et al., 2019).

An in-depth investigation of the mare deposits within the SPA basin could help provide valuable insights about the lunar mantle and crustal compositions. A comprehensive study of lunar surface rocks and basaltic melts certainly supplies information for its interior and its crust-mantle interaction mechanisms, improving the knowledge of the historical evolution of the Moon. In this work, we present a spectral analysis of Mare Ingenii. Starting from a morpho-stratigraphic map of the study area, we perform a mineralogical characterization based on spectral parameters derived from M^3 data. In Section 2 we present the data and methods used for mineralogical analysis. In Section 3 we present the results, which are then discussed in detail in Section 4. Concluding remarks are provided in Section 5.

2. Data Sets and Methods

We considered different data sets and techniques of analysis. Below, we describe in detail the selection of the Regions of Interest (ROIs), the geological mapping and the retrieval of the spectral parameters used for our analysis.

2.1. Data Sets for the Geological Mapping

To better characterize the geology of the area, we first produced a morpho-stratigraphic map of the Ingenii basin, namely a mapping product in which units are defined based on their morphology and relative stratigraphic position. Data used for this work include the Lunar Reconnaissance Orbiter Camera-Wide Angle Camera (LROC-WAC) (Robinson et al., 2010) mosaic with a spatial resolution of ∼100 m/pixel, the Lunar Reconnaissance Laser Altimeter (LOLA) and Kaguya Terrain Camera (TC) Digital Elevation Model (DEM), with a horizontal and vertical resolution of ∼59 m/pixel and 3–4 m, respectively (Barker et al., 2016). For our mapping, we then considered the Clementine Ultraviolet-Visible (UVVIS) Color Ratio mosaic (Lucey et al., 2000) for providing the geological characterization with a preliminary compositional discrimination of the different basin materials. The Clementine mosaic is a color basemap created by using different band ratios between three spectral filters equipped on the Clementine UVVIS camera (McEwen & Robinson, 1997). In particular, the red, green and blue channels correspond to the 750/415, 750/1,000, and 415/750 nm band ratios. The red channel identifies areas high in glass content and/or with a high degree of maturity, but it can also highlight areas with low titanium content. Iron-rich terrains are highlighted in green. Finally, the blue channel emphasizes high titanium contents

10.1029/2023JE007963

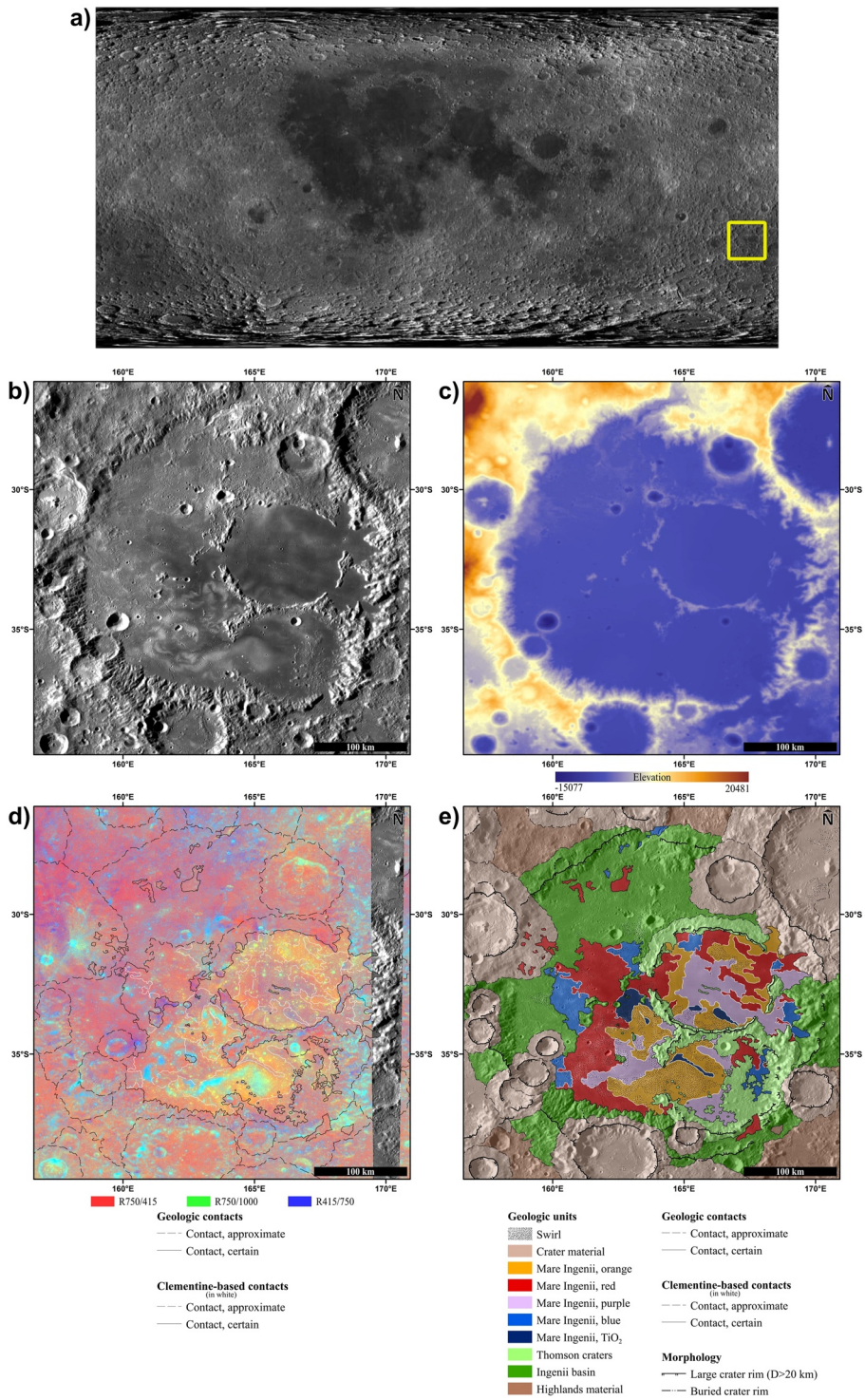

Figure 1. (a) Global morphology mosaic of the Moon (Lunar Reconnaissance Orbiter Camera-Wide Angle Camera [LROC-WAC]) with the yellow square indicating the location of Mare Ingenii and (b) detailed view of the Ingenii basin as from the LROC-WAC global mosaic (Robinson et al., 2010); (c) LRO-LOLA and Kaguya Terrain Camera Digital Elevation Model merged for the Ingenii basin (Barker et al., 2016); (d) Geological and Clementine-based contacts digitalization visualized on top the Clementine UVVIS Color Ratio mosaic (Lucey et al., 2000); (e) Morpho-stratigraphic map of the Ingenii basin region visualized on top of the LROC-WAC mosaic (Robinson et al., 2010). Units are shown with 50% of transparency. Refer to the text for the description of the units.

or bright albedos. The mapping was carried out using the *ESRI ArcGIS software*. Compared to the previously published global maps (Fortezzo et al., 2020; Ji et al., 2022), this map presents a greater detail on the area of interest and preliminarily integrates geology with multispectral information derived from color data.

2.2. Spectral Data Sets

We carried out a spectral analysis of Mare Ingenii by using hyperspectral data acquired by the Moon Mineralogy Mapper (M^3) onboard Chandrayaan-1. M^3 is an imaging spectrometer that operated in the visible and near-infrared 400–3,000 nm range. Ground sampling is nominally 140 m/pixel with 86 spectral channels providing an average spectral sampling of 30 nm (Pieters et al., 2009). The obtained data has been processed and downscaled to a spatial resolution of 600 m/pixel, a good compromise among map handling, computational time and quality of the results. We calibrated and photometrically corrected M^3 raw data set (Besse et al., 2013a, 2013b; Green et al., 2011), but photometric correction is sub-optimal in areas showing grazing solar illumination. We applied the Akimov function (Shkuratov et al., 1999) to improve the accuracy of the photometric correction. We then produced maps of the main spectral indices useful to investigate the mineralogy and the spectral characteristics or variations across Mare Ingenii basin.

2.3. Selection of the Regions of Interest (ROIs)

We selected ROIs by using the *ENVI image analysis software* (https://www.l3harrisgeospatial.com). The choice of the locations was driven by the reflectance variability and by the observation of surface features and morphological elements (i.e., hummocky regions showing rough aspects or smooth floors with plain material). ROIs were created by selecting several tens of pixels (from 30 to 120 points, depending on the ROI) on the raster layers and saved as ASCII text files. Spectra were acquired for each point and, subsequently, basic statistics (i.e., mean and standard deviation) were calculated for each ROI (see Table 1). Multiple spectra within a single region of interest were then averaged together, to obtain a representative spectrum of the ROI for all the investigated areas.

2.4. Spectral Parameters

Below we describe in detail the spectral indices considered for our analysis:

2.4.1. Reflectance at 580 nm (R580)

Reflectance variation is related to several factors, such as surface roughness, particle size, compositional variabilities and exposure to the space environment (i.e., space weathering) (Clark, 1983; Cloutis et al., 1986). With a visual geometric albedo of 0.12 (Rosenbush, 2005), the Moon surface appears quite dark if compared to other rocky planetary bodies. This is mainly due to the high concentrations of nanophase iron as a consequence of the space environment exposure (Pieters & Noble, 2016). Nevertheless, darker areas are observed in the basaltic maria and basins, dated as younger than the highlands, hence less affected by space weathering. In this case, the reflectance variations are driven by composition, specifically by mafic (i.e., Fe- and Mg-rich) minerals and opaque phases, which can be considered as darkening agents as largely observed also in laboratory spectra (e.g., Cloutis et al., 1986; Sunshine & Pieters, 1998; X. Zhang & Cloutis, 2021b). Combining the reflectance with other spectral parameters, such as spectral slope, band center and band depth, is a valuable tool to discriminate regions heavily affected by space weathering from those dominated by intrinsic mineralogical variations. Furthermore, a terrain's maturity partially characterizes the surface roughness and the spectral reflectance which emphasizes some morphological structures. Nevertheless, it can be closely associated with the grain size distribution, as a general increase in reflectance values is usually associated with a decrease in grain size (Clark, 1999). In this case, we selected the reflectance at 580 nm derived from M^3 data, which is close to the visible standard wavelength of 550 nm and safely unaffected by known or expected spectral signatures.

2.4.2. Absorption Band Centers

Most of the Moon NIR spectral features show two distinct absorption bands (often tagged as band I and band II), respectively centered at ∼1 and ∼2 μm (Adams, 1975; Burns, 1993), mainly due to the occurrence of pyroxenes (Denevi et al., 2007). Pyroxenes are the most abundant mineralogical phase on planetary surfaces, and their spectral behavior is strongly dominated by Fe^{2+} content in the M1 and M2 sites as well as by electronic transitions and ionic exchanges with other elements, especially Ca^{2+} and Mg^{2+}, in the crystallographic sites (Burns, 1993;

Journal of Geophysical Research: Planets

10.1029/2023JE007963

Table 1

Investigated Spectral Parameters (Mean Values ± Standard Deviation) for the Selected Regions of Interest Within the Ingenii Basin

Spectral parameters	R580	BCI (μm)	BDI (μm)	BCII (μm)	BDII (μm)	Band area ratio	Spectral slope (1/μm)	FeO (wt%)	TiO_2 (wt%)	R750/R580	R750/R1000	R580/R750
ROI 1 (dark material)	0.038 ± 0.003	0.974 ± 0.035	0.052 ± 0.021	2.033 ± 0.037	0.018 ± 0.008	1.411 ± 0.021	0.985 ± 0.063	11.86 ± 0.39	1.28 ± 0.03	1.269 ± 0.015	0.819 ± 0.015	0.788 ± 0.009
ROI 2 (dark material)	0.035 ± 0.002	0.985 ± 0.030	0.062 ± 0.017	2.077 ± 0.063	0.020 ± 0.008	1.422 ± 0.016	1.024 ± 0.039	12.29 ± 0.39	1.22 ± 0.03	1.266 ± 0.019	0.826 ± 0.020	0.790 ± 0.012
ROI 3 (dark material)	0.036 ± 0.002	0.982 ± 0.055	0.061 ± 0.030	2.078 ± 0.088	0.018 ± 0.015	1.409 ± 0.028	0.945 ± 0.038	12.44 ± 0.37	1.23 ± 0.03	1.259 ± 0.035	0.829 ± 0.031	0.795 ± 0.023
ROI 4 (dark material)	0.036 ± 0.001	0.961 ± 0.032	0.061 ± 0.025	2.091 ± 0.067	0.023 ± 0.012	1.415 ± 0.035	0.946 ± 0.035	12.41 ± 0.29	1.23 ± 0.02	1.273 ± 0.022	0.839 ± 0.017	0.786 ± 0.014
ROI 5 (dark material)	0.040 ± 0.002	0.988 ± 0.029	0.075 ± 0.025	2.121 ± 0.042	0.044 ± 0.013	1.388 ± 0.027	0.928 ± 0.046	11.82 ± 0.29	1.18 ± 0.02	1.260 ± 0.021	0.854 ± 0.023	0.794 ± 0.013
ROI 6 (dark material)	0.039 ± 0.002	0.979 ± 0.019	0.067 ± 0.018	2.080 ± 0.031	0.023 ± 0.009	1.411 ± 0.017	0.932 ± 0.033	12.05 ± 0.26	1.20 ± 0.02	1.268 ± 0.021	0.844 ± 0.019	0.789 ± 0.013
ROI 7 (dark material)	0.038 ± 0.002	0.981 ± 0.036	0.054 ± 0.022	2.038 ± 0.079	0.019 ± 0.010	1.417 ± 0.030	0.944 ± 0.035	11.93 ± 0.24	1.19 ± 0.02	1.274 ± 0.019	0.828 ± 0.022	0.785 ± 0.012
ROI 8 (dark material)	0.041 ± 0.004	0.993 ± 0.043	0.061 ± 0.022	2.075 ± 0.040	0.030 ± 0.011	1.415 ± 0.035	0.904 ± 0.053	11.81 ± 0.38	1.18 ± 0.03	1.263 ± 0.024	0.853 ± 0.024	0.792 ± 0.015
ROI 9 (dark material)	0.048 ± 0.004	0.958 ± 0.027	0.066 ± 0.034	2.095 ± 0.063	0.045 ± 0.026	1.368 ± 0.039	0.875 ± 0.071	10.62 ± 0.36	1.10 ± 0.02	1.253 ± 0.020	0.847 ± 0.044	0.798 ± 0.012
ROI 10 (dark material)	0.043 ± 0.002	0.965 ± 0.043	0.054 ± 0.023	2.103 ± 0.044	0.035 ± 0.012	1.400 ± 0.054	0.922 ± 0.059	11.32 ± 0.24	1.15 ± 0.02	1.248 ± 0.021	0.834 ± 0.023	0.801 ± 0.013
ROI 11 (dark material)	0.040 ± 0.003	0.985 ± 0.032	0.045 ± 0.020	2.087 ± 0.069	0.016 ± 0.007	1.408 ± 0.019	0.954 ± 0.046	11.58 ± 0.35	1.17 ± 0.03	1.264 ± 0.023	0.827 ± 0.020	0.791 ± 0.014
ROI 12 (swirl material)	0.060 ± 0.004	0.978 ± 0.027	0.081 ± 0.024	2.112 ± 0.022	0.047 ± 0.012	1.361 ± 0.053	0.670 ± 0.034	10.64 ± 0.29	1.10 ± 0.02	1.225 ± 0.013	0.914 ± 0.025	0.816 ± 0.008
ROI 13 (swirl material)	0.077 ± 0.003	0.962 ± 0.009	0.065 ± 0.022	2.066 ± 0.030	0.040 ± 0.011	1.348 ± 0.026	0.564 ± 0.027	9.61 ± 0.27	1.04 ± 0.02	1.189 ± 0.016	0.923 ± 0.023	0.841 ± 0.012
ROI 16 (swirl material)	0.058 ± 0.002	0.966 ± 0.013	0.072 ± 0.017	2.079 ± 0.032	0.039 ± 0.009	1.355 ± 0.025	0.751 ± 0.026	9.94 ± 0.20	1.06 ± 0.01	1.264 ± 0.014	0.878 ± 0.017	0.791 ± 0.009
ROI 17 (swirl material)	0.056 ± 0.003	0.960 ± 0.011	0.062 ± 0.022	2.072 ± 0.026	0.041 ± 0.014	1.358 ± 0.036	0.772 ± 0.054	10.21 ± 0.20	1.08 ± 0.01	1.256 ± 0.014	0.866 ± 0.023	0.796 ± 0.009
ROI 14 (intermediate m.)	0.068 ± 0.006	0.961 ± 0.016	0.037 ± 0.017	2.008 ± 0.052	0.022 ± 0.013	1.356 ± 0.014	0.687 ± 0.039	9.03 ± 0.61	1.00 ± 0.04	1.254 ± 0.010	0.851 ± 0.024	0.798 ± 0.006
ROI 15 (intermediate m.)	0.056 ± 0.006	0.938 ± 0.022	0.032 ± 0.017	1.981 ± 0.049	0.019 ± 0.011	1.367 ± 0.036	0.756 ± 0.059	10.35 ± 0.44	1.09 ± 0.03	1.245 ± 0.016	0.830 ± 0.017	0.803 ± 0.010
ROI 18 (bright material)	0.116 ± 0.011	0.928 ± 0.016	0.105 ± 0.028	1.963 ± 0.022	0.079 ± 0.024	1.659 ± 0.276	0.437 ± 0.065	7.07 ± 0.53	0.89 ± 0.03	1.200 ± 0.021	0.933 ± 0.028	0.834 ± 0.014
ROI 19 (bright material)	0.081 ± 0.006	0.912 ± 0.014	0.043 ± 0.024	2.042 ± 0.019	0.067 ± 0.019	1.310 ± 0.104	0.658 ± 0.059	8.16 ± 0.29	0.95 ± 0.02	1.220 ± 0.011	0.865 ± 0.021	0.820 ± 0.007
ROI 20 (bright material)	0.156 ± 0.015	0.913 ± 0.025	0.059 ± 0.038	1.950 ± 0.055	0.057 ± 0.032	1.532 ± 0.183	0.305 ± 0.056	6.27 ± 0.63	0.85 ± 0.03	1.144 ± 0.018	0.924 ± 0.034	0.875 ± 0.014
ROI 21 (bright material)	0.126 ± 0.009	0.940 ± 0.009	0.068 ± 0.023	1.970 ± 0.063	0.050 ± 0.019	1.424 ± 0.151	0.424 ± 0.058	6.37 ± 0.70	0.86 ± 0.04	1.204 ± 0.013	0.913 ± 0.027	0.831 ± 0.009
ROI 22 (bright material)	0.102 ± 0.012	0.935 ± 0.007	0.075 ± 0.033	1.968 ± 0.032	0.055 ± 0.032	1.463 ± 0.251	0.480 ± 0.073	7.64 ± 0.80	0.92 ± 0.05	1.208 ± 0.014	0.906 ± 0.042	0.828 ± 0.010
ROI 23 (bright material)	0.119 ± 0.014	0.928 ± 0.017	0.059 ± 0.055	1.976 ± 0.053	0.059 ± 0.046	1.523 ± 0.302	0.401 ± 0.069	7.24 ± 0.95	0.90 ± 0.05	1.187 ± 0.024	0.911 ± 0.051	0.843 ± 0.017
ROI 24 (bright material)	0.113 ± 0.008	0.925 ± 0.009	0.053 ± 0.018	1.951 ± 0.027	0.049 ± 0.016	1.388 ± 0.134	0.466 ± 0.030	6.91 ± 0.43	0.88 ± 0.02	1.203 ± 0.010	0.889 ± 0.016	0.832 ± 0.007
ROI 25 (bright material)	0.114 ± 0.007	0.924 ± 0.016	0.069 ± 0.033	1.982 ± 0.029	0.066 ± 0.029	1.463 ± 0.234	0.455 ± 0.049	7.05 ± 0.40	0.89 ± 0.02	1.198 ± 0.014	0.913 ± 0.031	0.835 ± 0.010

Table 1
Continued

Spectral parameters	R580	BCI (μm)	BDI (μm)	BCII (μm)	BDII (μm)	Band area ratio	Spectral slope (1/μm)	FeO (wt%)	TiO_2 (wt%)	R750/R580	R750/R1000	R580/R750
ROI 26 (bright material)	0.143 ± 0.014	0.911 ± 0.019	0.058 ± 0.051	1.927 ± 0.042	0.051 ± 0.046	1.498 ± 0.269	0.412 ± 0.059	5.42 ± 0.89	0.81 ± 0.05	1.186 ± 0.019	0.886 ± 0.035	0.843 ± 0.014
ROI 27 (bright material)	0.131 ± 0.012	0.936 ± 0.017	0.111 ± 0.041	1.973 ± 0.046	0.127 ± 0.039	1.742 ± 0.245	0.436 ± 0.066	5.80 ± 0.95	0.83 ± 0.05	1.210 ± 0.012	0.930 ± 0.053	0.826 ± 0.008
ROI 28 (bright material)	0.141 ± 0.011	0.918 ± 0.020	0.072 ± 0.038	1.913 ± 0.041	0.074 ± 0.036	1.519 ± 0.246	0.457 ± 0.074	4.96 ± 0.64	0.79 ± 0.03	1.216 ± 0.022	0.893 ± 0.030	0.823 ± 0.015

Note. Refer to the main text for ROI details (see Section 2.3).

Denevi et al., 2007). Nevertheless, other mineralogical phases present absorptions associated to Fe^{2+} in similar spectral regions, but they are not relevant for the Moon, with the exception of spinels (e.g., chromite; Cloutis et al., 2004). Band centers are useful to identify the mineralogical phases associated with the absorption band and, furthermore, they are sensitive to compositional variations within minerals. Laboratory studies revealed that pyroxenes absorption at 1 and 2 μm are shifted toward longer wavelengths for increasing Fe^{2+} and Ca^{2+} abundance (Cloutis, 2002; Gaffey, 1976; Klima et al., 2007, 2011), even though similar shifts could be linked to the presence of mineralogical phases within rocks such as olivine, spinel, plagioclase, or glasses. To calculate the 1- and 2-μm band center positions, we first removed the continuum dividing the reflectance spectra by the line connecting the two band shoulders, then we considered as band center the wavelength corresponding to the minimum of the 2nd polynomial fitting the region around the band center (see Clark, 1999; Cloutis et al., 1986).

2.4.3. Absorption Band Depths

Absorption band depth is usually sensitive to mineralogical abundances (e.g., pyroxenes, olivine and opaque minerals) as well as to grain size and space weathering (Adams, 1974; Burns, 1970; Clark, 1999; Serventi et al., 2013). Indeed, the band depth also depends on the maturity of the soils, as occurrence of iron nanophases (formed due to the prolonged exposure time) tend to reduce the reflectance and the absorption band depths (Clark, 1983; Pieters et al., 2012). Moreover, coarse-grained lithologies generally produce deeper absorption bands than very fine-grained lithologies (Horgan et al., 2014; King & Ridley, 1987), since finer size particles exhibit higher specific surface which is able to reflect. For this reason, in fine-grained lithologies reflectance increases with decreasing particle size (Sun et al., 2016). We calculated the band depth considering the method used by Clark and Roush (1984).

2.4.4. Absorption Band Area Ratio

The band area ratio (BAR) is defined as the ratio between the band II and band I area (Cloutis et al., 1986). It is used for investigating the spatial distribution of olivine on planetary surfaces (Cloutis et al., 1986). Olivine spectra exhibit a broad and asymmetric absorption band centered near 1.05 μm, and no 2 μm band (e.g., Horgan et al., 2014). Consequently, low (i.e., <1) BAR values indicate the possible presence of olivine (both forsteritic and fayalitic end-members) in pyroxenes mixtures (Adams, 1974; Cloutis et al., 1986; X. Zhang & Cloutis, 2021a, 2021b).

2.4.5. Global Spectral Slope

Moon spectra show steep ("red") spectral slope (reflectance increases with increasing wavelengths).

This parameter is influenced by several effects, such as the production of nFe0 particles caused by space weathering effects inducing a spectral reddening (Pieters & Noble, 2016), the terrain maturity, the composition and the grain size variations (Clark, 1999; Cloutis et al., 1986). Since the lunar surface is strongly affected by space weathering, it is a key parameter to describe the spectral variations occurring on the Moon. We calculated the spectral slope between ~0.3 and 1.0 μm adopting the method described by Cuzzi et al. (2009), and Filacchione et al. (2012).

2.4.6. FeO and TiO_2 (wt%) Content

FeO and TiO_2 are often considered along with other spectral parameters as they are very abundant in volcanic rocks, which are commonly found on planetary surfaces. High occurrence of these elements might reveal a mafic signature in the investigated areas and, for this reason, they are considered as geochemical tracers for unraveling the emplacements of the basaltic plains. To retrieve the FeO and TiO_2 (in wt%), we considered the first method described by Zhang (2014), developed for M^3 data. Note that the methods available in literature to derive the abundances of FeO and TiO_2 use different data sets, showing a comparable distribution, but some discrepancies in terms of absolute values (Lucey et al., 2000; Sato et al., 2017; W. Zhang, 2014).

3. Results

All the investigated spectral parameters are reported in Table 1 and are described below.

3.1. Geology of the Ingenii Basin Area

Figure 1e shows the morpho-stratigraphic map integrated with multispectral color information produced for our study area.

In its interior, the Ingenii basin presents a large smooth plain characterized by the presence of a high albedo lunar swirl. The plain is mostly confined within the Thomson and ThomsonM crater rims but it also encroaches on the Ingenii basin's bumpy floor (i.e., included within the Ingenii basin unit, as from Figure 1e), covering part of it. Several younger craters larger than 20 km in diameter superimpose to the basin and their ejecta deposits partly cover the floor of Ingenii, contributing to its rough appearance.

Following the Clementine color composite map, the Ingenii basin area reflects the widespread presence of mature highland material enriched in glass content (high 750/415 nm ratio), anorthosites and/or bright albedo scarps (high 415/750 nm ratio) characterizing the rough materials and crater deposits covering the area outside of basaltic plain of Mare Ingenii (i.e., Ingenii basin, Thomson craters, Crater material and Highland material units, see Figure 1e).

In particular, we observe that the smooth plain of Mare Ingenii is characterized by different hues of color (see in detail Figure 1e). Some areas display a bluer color (higher 415/750 nm ratio) probably reflecting the presence of a thin anorthositic coating of crater-ejected material (i.e., Mare Ingenii, blue unit, as from Figure 1e) while even bluer areas present a good correlation with titanium enriched basalts as estimated by Sato et al. (2017) (i.e., Mare Ingenii, TiO_2 unit, as from Figure 1e). However, most of the mare shows a red-to-orange color (higher 750/1,000 nm ratio) indicating a low-titanium basaltic plain and/or the presence of abundant glasses. The slight color difference, from red (i.e., Mare Ingenii, red unit, as from Figure 1e) to orange (i.e., Mare Ingenii, orange unit, as from Figure 1e), is probably caused by the bright albedo of the swirl material which might influence the units color ratio and result in a lighter color hue. The remaining areas still present a prevalent redder color (high 750/415 nm ratio) but influenced by a bluer component indicative of low-to-medium titanium basalts (i.e., Mare Ingenii, purple unit, as from Figure 1e).

3.2. Selected ROIs

Based on the morpho-stratigraphic analysis, the spectral variability and visible reflectance, we identified several Regions Of Interest (ROIs, Figure 2). A total of 28 ROIs have been selected in different regional contexts and classified as followed:

1. Dark material, namely mare regions *sensu stricto* (basaltic low reflectance smooth plains): from ROI 1 to ROI 11;
2. Swirl material (showing sinuous and heterogeneous aspect with intermediate reflectance values): ROI 12, ROI 13, ROI 16, and ROI 17;
3. Intermediate regions (showing intermediate albedo values, likely indicating heterogeneous material): ROI 14, which seems to be located on a very thin coating of ejecta deposits coming from a very small secondary craters, and ROI 15, located on rough pre-mare deposits of Thomson M crater;
4. Bright material (small craters): ROI 18 and ROI 19 have been selected as strictly within Thomson M impact crater, but nine additional ROIs (i.e., from ROI 20 to ROI 28) have been selected on the surrounding terrains for a more extensive comparison.

3.3. Reflectance at 580 nm (R580)

Thomson craters within the Ingenii basin are made up of a dark and smooth mare floor (i.e., ROI 1 to ROI 11; Figure 3a; Figures 4a and 4b) and clearly show the lowest values of reflectance (R580 ~0.04–0.05) if compared to the overall regional setting. The NW highlands, instead, exhibit the highest reflectance values (from ~0.08 to ~0.13) and nearly resemble the range of the bright material (ROI 18 to ROI 28) within small craters (~0.08–0.16). Finally, the swirl (ROI 12, ROI 13, ROI 16, ROI 17) and intermediate regions (ROI 14 and ROI 15) show medium reflectance values of ~0.06–0.08; Figures 5c and 5d).

3.4. Absorption Band Centers

The spectral distribution maps of the band centers are shown in Figures 3c and 3d. The four ROIs groups generally appear to be well distinguished, with only rare overlaps (Figure 5a). Dark material (most notably mare deposits) shows the pyroxene absorption band center positions near 1 and 2 μm (hereafter, BCI and BCII) shifted to longer wavelengths, that is, BCI = 0.96–0.99 μm and BCII = 2.03–2.12 μm, respectively. On the other hand,

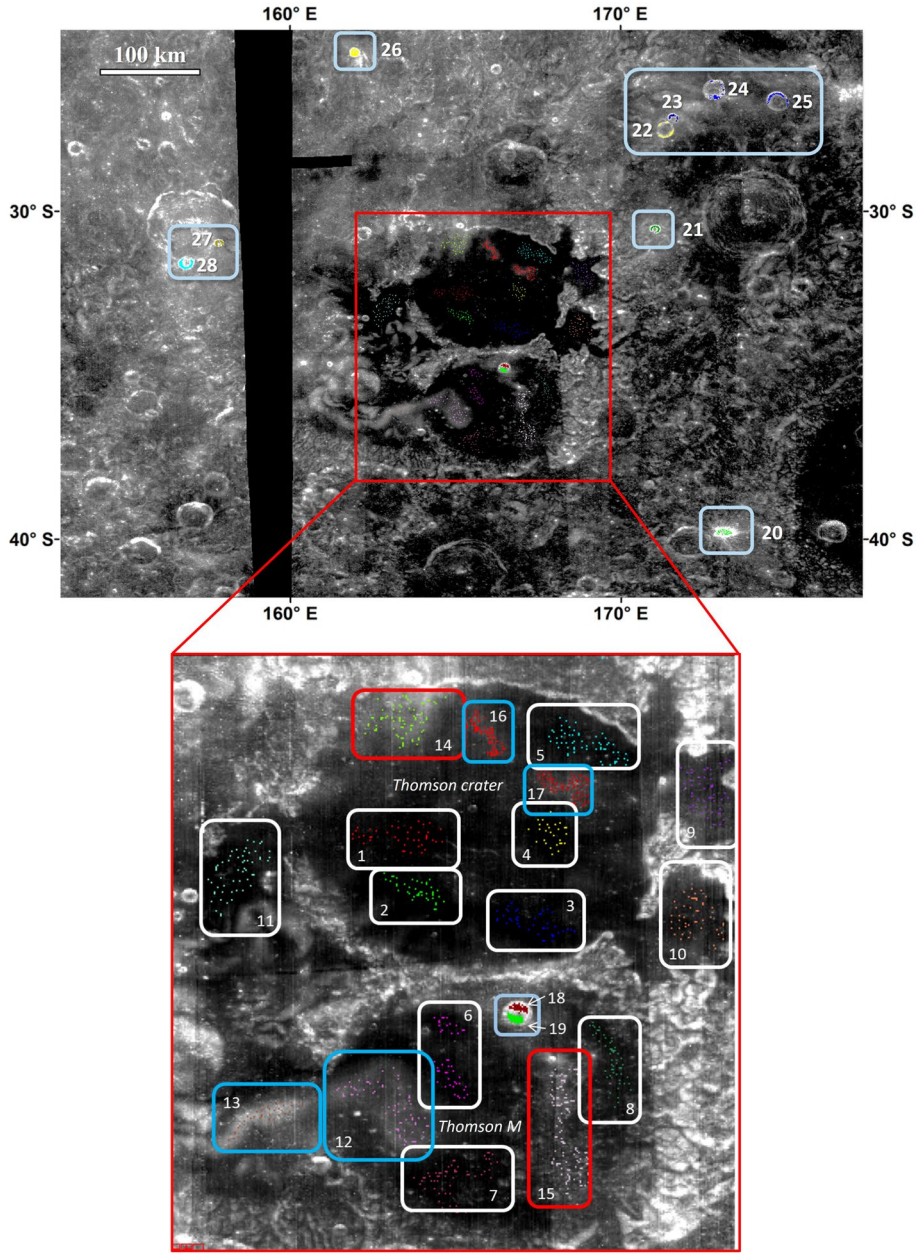

Figure 2. Reflectance map at 580 nm of the Ingenii basin showing the locations of the selected Regions of Interest (ROIs). See the main text for the subdivision and colors in detail of the ROIs (white squares indicate the dark material within the maria floor of the Thomson craters; cyan squares indicate the swirl regions; red squares indicate intermediate regions and light blue squares are for bright materials.

the swirl region shows peculiar morphologies and reflectance similar to the intermediate regions, with typical values of BCI = 0.96–0.98 μm and BCII = 2.07–2.11 μm. Intermediate areas exhibit slightly lower values (i.e., BCI = 0.94–0.96 μm and BCII = 1.98–2.01 μm), whereas bright material of the small craters show the lowest band centers values (BCI = 0.91–0.94 μm and BCII = 1.91–2.04 μm). A general increase in the band center wavelengths is then observed from bright material to dark mare deposits, which reflects compositional variations. Different from the other bright materials, the continuum removed spectrum of ROI 19 (small bright crater in the northern part of Thomson M crater; Figures 4g and 4h) shows anomalous features exhibiting a band II center shifted toward much longer wavelengths. Moreover, even though the absorption band centers appear to be scattered if plotted with the absorption band depths, they clearly exhibit some correlations with other main parameters, such as FeO, TiO_2, R580 and spectral slope; Figures 5e, 5f, and 5h).

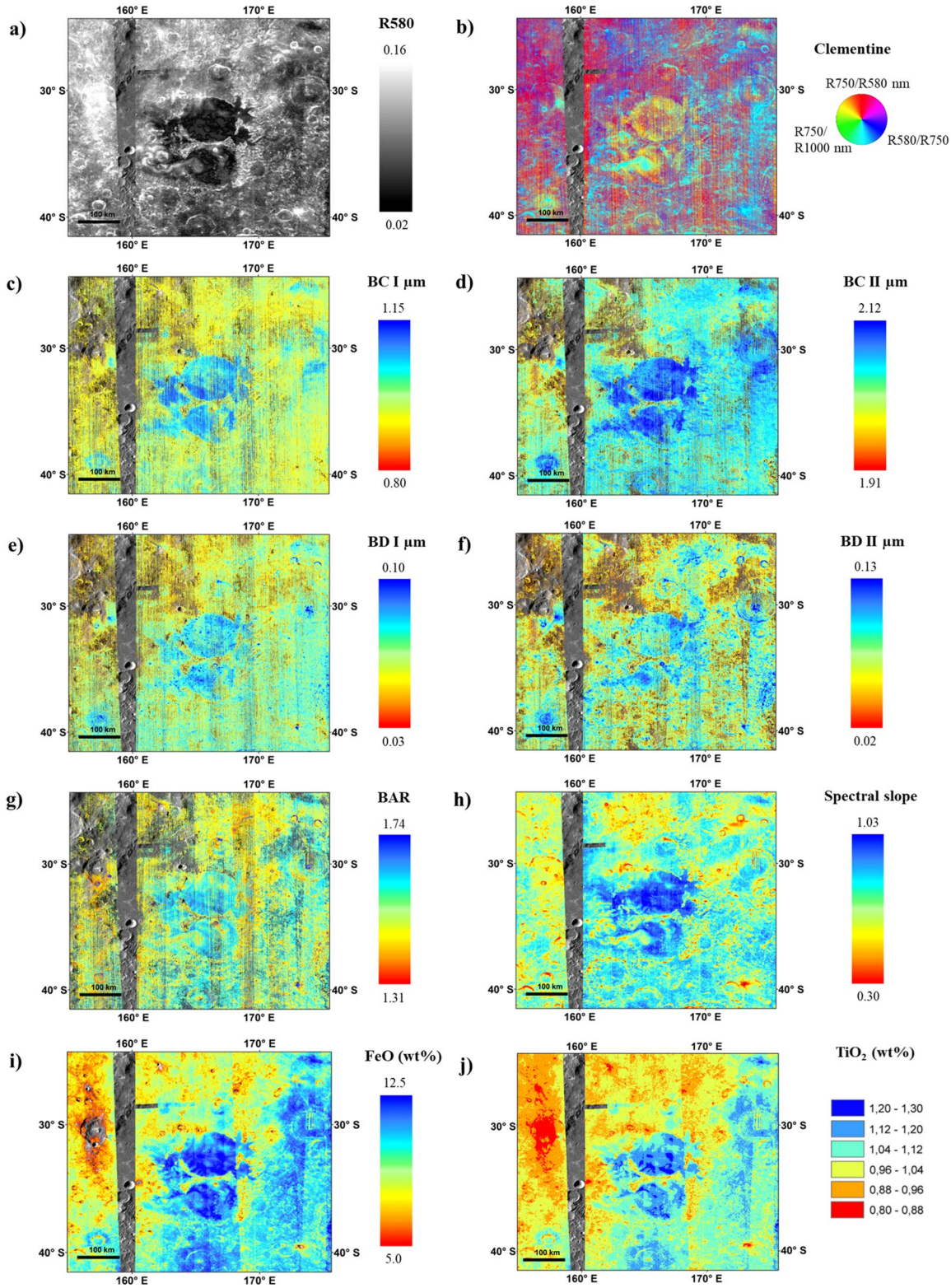

Figure 3. Investigated spectral parameters maps. (a) Reflectance at 580 nm (R580 nm); (b) RGB "Clementine-like" color composite mosaic, R: 750 nm/580 nm G: 750 nm/1000 nm and (b) 580 nm/750 nm; (c, d) Spectral maps of band center at 1 and 2 micron, respectively; (e, f) Spectral maps of band depth at 1 and 2 micron; (g) Band area ratio spectral map; (h) Global spectral slope map; (i, j) FeO and TiO_2 abundance maps (expressed in wt %).

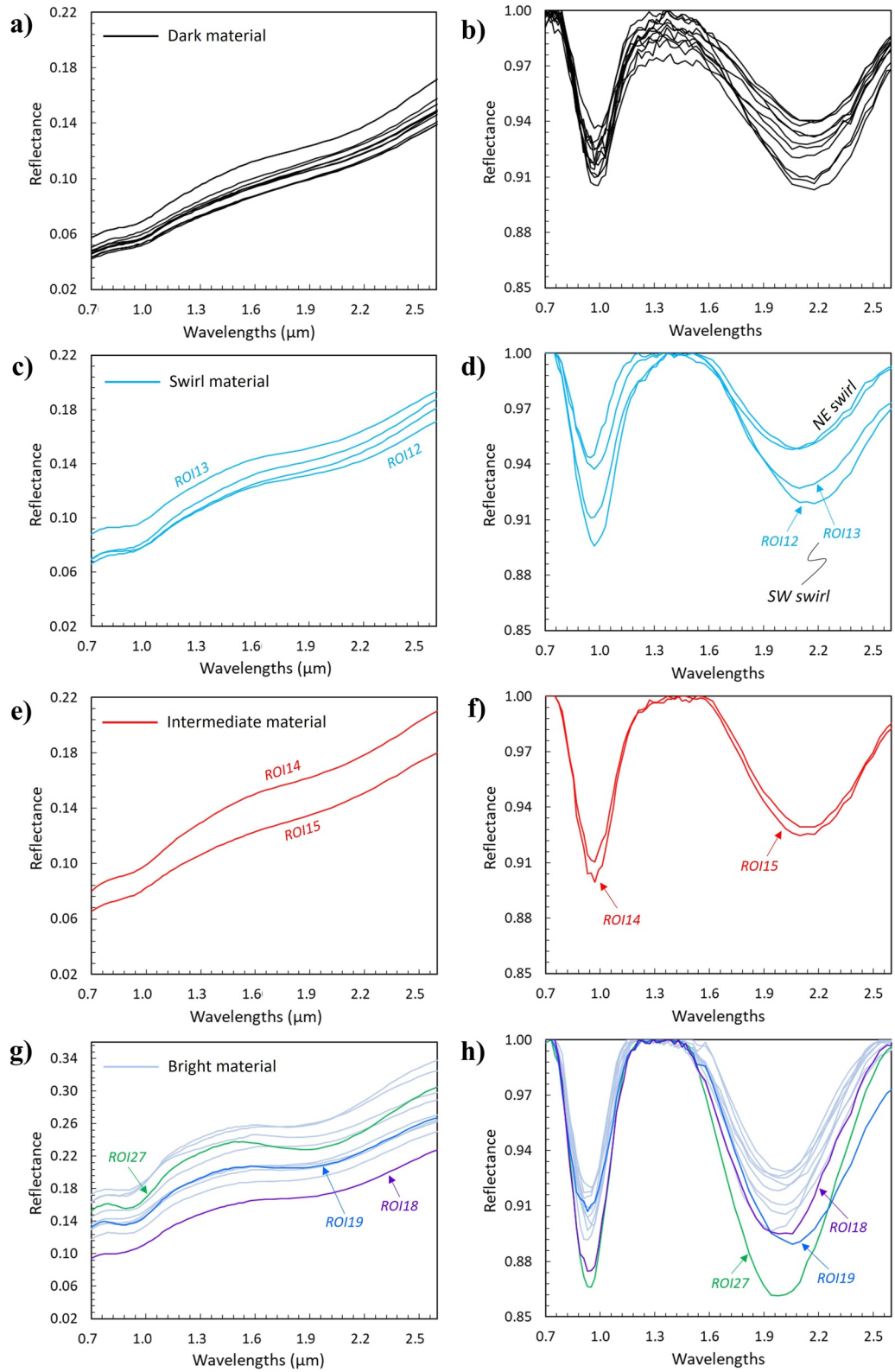

Figure 4. Average spectra (left panels) and continuum removed spectra (right panels) of investigated Regions of Interest (ROIs) for (a, b) dark material (i.e., from ROI 1 to ROI 11), (c, d) swirl regions (i.e., ROI 12-13-16-17), (e, f) intermediate material (ROI 14 and ROI 15), and (g, h) bright material (from ROI 18 to ROI 28). Note: on left panels, the bright materials have a larger reflectance range.

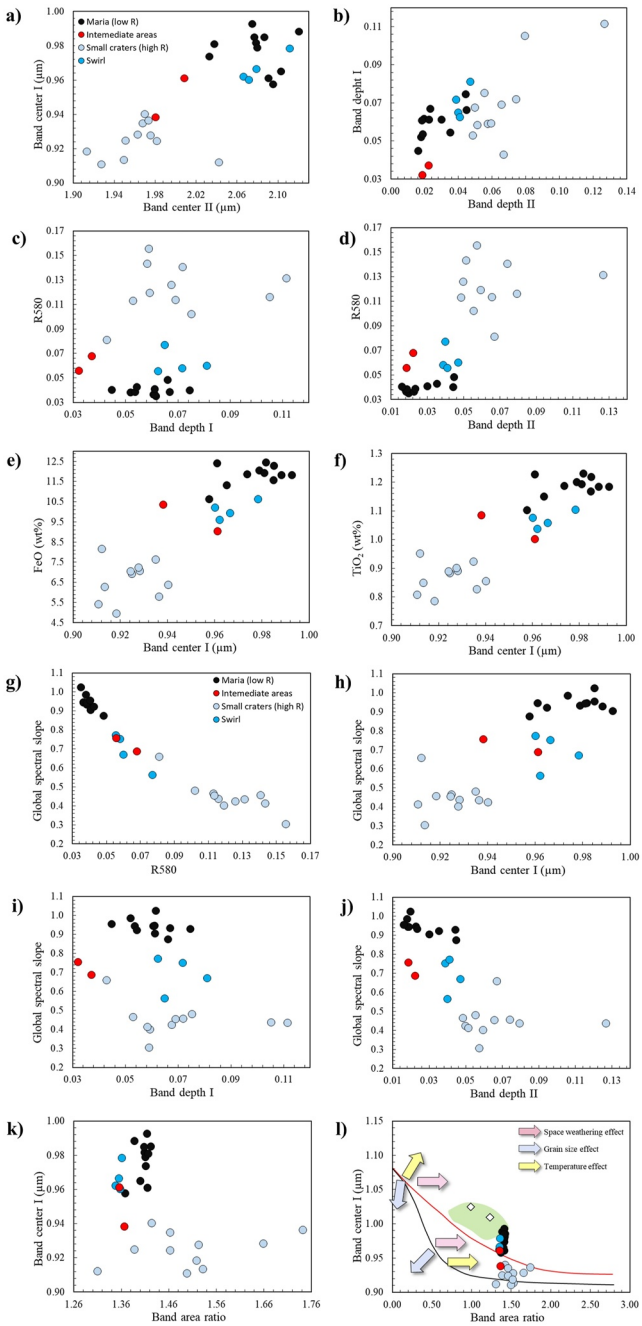

Figure 5. Spectral parameter plots for Ingenii basin investigated Regions of Interest. (a) Band center at 1 μm versus band center at 2 μm. (b) Band depth at 1 μm versus band depth at 2 μm. (c) Reflectance at 580 nm versus band depth at 1 μm and versus (d) band depth at 2 μm. (e) FeO and (f) TiO_2 versus band center at 1 μm. (g) Global spectral slope versus reflectance at 580 nm, versus (h) band center at 1 μm, versus (i) band depth at 1 μm, and versus (j) band depth at 2 μm. (k) Band center at 1 micron versus band area ratio, compared in panel (l)) with ol-opx mixtures line (of terrestrial materials) from Cloutis et al., 1986 (black line) and with ol-cpx-opx mixtures from X. Zhang and Cloutis (2021b) (red line). Green field is overall compositions from other maria in the South Pole-Aitken basin (from X. Zhang et al. (2019)), whereas open diamonds represent Ilmenite-rich basalts from X. Zhang and Cloutis (2021b).

3.5. Absorption Band Depths

We calculated the absorption band depths of the material composing the investigated ROIs (Figures 3e and 3f) to identify their compositional variations and mineralogical phase abundances (Figures 5b–5d). Dark material spectra (Figures 4a and 4b) exhibit rather low band depth values (BDI = 0.03–0.08 and BDII = 0.02–0.05), always comprising the range of the swirl and intermediate regions (Figures 4c–4f). Bright material absorption bands (respectively BDI = 0.04–0.08 and BDII = 0.05–0.08; Figures 4g and 4h) seem comparable to other investigated spectra. Indeed, all the spectra show strong band II depth, but the band I of ROI 19 spectrum (Figure 4h) is weaker with respect to the band II. Quite similar behavior can be also observed for the spectrum of ROI 27 bright material (a small crater located on the western rim of Ingenii rim; see Figure 4h), which in addition definitely exhibits the deepest absorption values of the whole range (i.e., BDI = 0.11 and BDII = 0.13). Finally, we observe an anticorrelation between band II depths and global slopes (Figure 5j).

3.6. Absorption Band Area Ratio

Following the approach of Gaffey et al. (1993) and Carli et al. (2018), we compared the BAR values (Figure 3g) with band I center positions (Figures 5k and 5l). We find no clear correlations, even though BAR shows distinct trends for two end-members (namely, bright and dark material). Indeed, BAR is restricted to a very narrow range of values (i.e., 1.31–1.74, see Figure 5k), and looking to the inset (Figure 5l) one can notice that for the dark material, swirl and intermediate regions BAR values range between 1.35 and 1.42 and BCI between 0.96 and 0.99, defining a cluster separated by the bright material. Bright materials are characterized by the highest BAR values, varying from 1.31 to 1.74 (with BCI values from 0.91 to 0.94), likely indicating a predominance for minerals with significant 2-μm band absorption (e.g., pyroxenes). Indeed, ROI 19 and ROI 27 exhibit the lowest (~1.31) and the highest (~1.74) BAR value, respectively, representing the two endmembers within the variation range of the bright materials and likely indicating that their spectral characteristics might be related to several factors and not only to mineralogical variations.

3.7. Global Spectral Slope

The global spectral slope is a useful parameter to infer the maturity of the terrains, since it is affected by space weathering processes. The Ingenii basin spectral slope is anticorrelated with the reflectance (Figure 5g) and the absorption depths (Figures 5i and 5j), whereas it increases with increasing absorption band center wavelengths (Figure 5h). Dark material within Thomson craters shows the highest spectral slope values (i.e., 0.88–1.02; Figure 3h), with the mare basaltic floor being younger than the surrounding highlands, which exhibit a typical red slope. This clearly indicates that space weathering is not the only process affecting the Ingenii basin. Intermediate regions show spectral slope values between 0.69 and 0.76 and result close to the field of the swirl material (overall range ~0.56–0.77). Notably, northeast swirl ROIs (namely, ROI 16–17) exhibit higher values (i.e., 0.75–0.77) respect than south-west swirl ROIs (ROI 12–13) which instead show a neutral slope. Such features likely indicate that swirl material is younger than the surrounding highlands. The space weathering strongly affects the spectral features, reducing the reflectance and the depth of the absorption bands

(Pieters & Noble, 2016), showing a typical spectral reddening characteristic of mature terrains. On the other hand, the bright materials exhibit a "blue" global spectral slope (i.e., 0.30–0.48, with ROI 19 up to 0.66), likely representing fresh craters materials.

3.8. FeO and TiO_2 (wt%) Content

FeO content is usually correlated with TiO_2 amount (see Figures 3i, 3j, 5e, and 5f). The highest abundances for FeO (~10.6–12.4 wt%) and TiO_2 (~1.1–1.2 wt%) are observed in the dark material of the maria floors of both Thomson craters (ROI 1 to ROI 11). On the other hand, iron and titanium content seem to decrease toward swirl (ROI 12-13-16-17) and intermediate regions (ROI 14 and ROI 15) showing similar range of values (i.e., overall FeO = 9.0–10.6 wt% and TiO_2 = 1.0–1.1 wt%), down to the lowest values with the small craters bright material (respectively, ~5.0–8.2 and ~0.8–1.0 wt%, ROI 18 to ROI 28). This trend indeed reflects the positive correlation that absorption band center values exhibit with both FeO and TiO_2 abundances. Differently, these oxides show a rough negative correlation if plotted versus absorption band depth at 2 μm (and scattered trends vs. absorption band depth at 1 μm).

4. Discussion

The analysis of M^3 data reveals that the Ingenii basin is characterized by a substantial spectral variability (Figures 3–5). We selected a large part of the ROIs within Thomson craters, with the aim of characterizing spectral properties of the mare flood plain and trying to infer the mineralogical compositions of the basaltic floor. To achieve this goal, we used diagnostic spectral parameters (e.g., absorption band centers, band depths, etc.) as they are indicative of iron-rich phase abundances (i.e., pyroxenes, olivine or opaques) as well as grain size distributions. On the other hand, other spectral indices (e.g., reflectance, spectral slope) are more useful for inferring the surface roughness and the maturity of the investigated area.

4.1. Spectral Features of the Investigated ROIs

Near-infrared reflectance spectra of the ROIs area chiefly show two absorption bands centered at about 1 and 2 μm. For a more comprehensive analysis, we compared Ingenii basin spectral parameters with some analogs selected from NASA Reflectance Experiment LABoratory database (*RELAB*, Klima et al., 2007, 2011) pyroxenes laboratory spectra. Generally, Mg-Fe pyroxenes (i.e., orthopyroxenes) spectra are characterized by a relatively narrow and symmetric absorption band at ~0.9 μm, as well as a broad and asymmetric absorption band near ~1.9 μm (Adams, 1974; Horgan et al., 2014). Moreover, absorption band centers positions are shifted toward longer wavelengths with the increasing of Fe^{2+} and Ca^{2+} content. The absorption depth usually shows a distinct and linear correlation with iron content (Klima et al., 2007), showing very deep and prominent bands for compositions close to ferrosilite end-member. Yet when the contribution of calcic components starts to prevail within crystallographic sites, the correlation between absorption band centers positions and FeO abundances is no longer evident. Variations in CaO content seem to be predominant in the definition of the absorption band centers positions, suggesting that this element strongly controls the spectral signature (Klima et al., 2011). Indeed, Ca-Mg-Fe pyroxenes (i.e., clinopyroxenes) exhibit very complex and various spectral features mostly depending on the chemical different content in the mineral structures. Low-Ca clinopyroxenes (i.e., pigeonite, $\sim Wo_{5-20}$; Klima et al., 2011) always show two well-defined absorption bands centered near 1 and 2 μm (Adams, 1974; Klima et al., 2011), unlike Ca-free pyroxenes (i.e., enstatite and ferrosilite) which show absorption band positions moving toward longer wavelengths up to Ca-rich compositions $\sim Wo_{30-35}$ (i.e., augite). Conversely, Ca-saturated pyroxenes (i.e., diopside and hedenbergite, $\sim Wo_{40-50}$) show more complex spectral features (Adams, 1974) with absorptions drastically decreasing at 2 μm, nearly disappearing (Klima et al., 2011).

Mare Ingenii's investigated parameters recall the above-mentioned characteristics, both Ca-free and low-Ca pyroxenes groups. Dark material, swirl and intermediate regions show rather comparable spectral features with absorption band centers positions decreasing from dark material from swirl to intermediate regions (see Figure 5a) and likely resembling the Ca-rich pyroxenes spectral signature (Figure 6). In particular, if we compare absorption band centers positions of these ROIs with laboratory pyroxenes values, we note that swirl and intermediate regions parameters are close to low-Ca clinopyroxenes (Figure 6), more specifically to compositions close to pigeonite (Klima et al., 2011). On the other hand, bright material of small craters always distinguish from

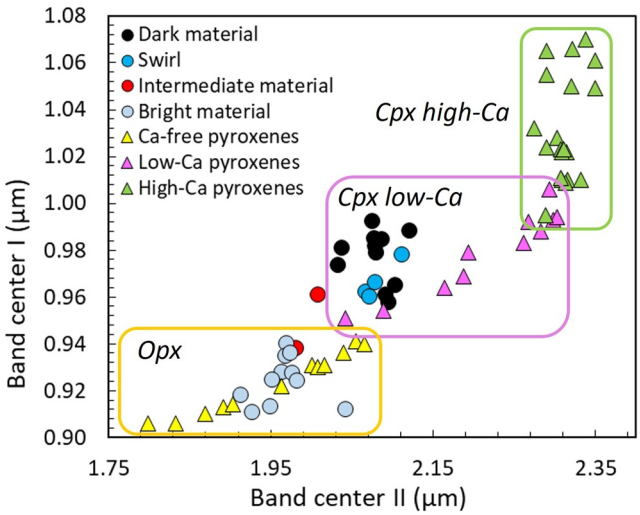

Figure 6. Absorption band center 1 μm versus absorption band center 2 μm of the investigated Regions of Interest within Mare Ingenii basin. Band centers of Ca-free and Ca-bearing pyroxenes (Klima et al., 2007, 2011) have been plotted for a comparison.

other investigated areas, as also their spectra definitely show evident absorption features at 1 and 2 μm, which diverge from other quite flat patterns (Figure 4g). The continuum removed spectra of the bright material are characterized by deep absorption of the bands (Figure 4h) and they clearly show absorption band center positions shifted toward shorter wavelengths, which mostly resemble orthopyroxenes (i.e., Ca-free pyroxenes; Figure 6) compositions and more specifically Mg- and Fe-medium rich compositions (i.e., $Mg_{35–75}$; Klima et al., 2007).

Nevertheless, there are some limitations about dealing with synthetic material. Indeed, in order to simplify the laboratory spectral systematics, Klima et al. (2011) focused on synthetic pyroxenes only considering Mg^{2+}, Fe^{2+}, and Ca^{2+} cations and excluded important elements (such as Al, Na or Mn), so this constraint certainly does not reflect the natural pyroxenes compositions. Minerals do not occur on planetary surfaces as pure and single phases unlike laboratory investigations which represent synthetic pure compositions. Anyway, pyroxene bands are typically prominent and well developed, often dominating the spectral features of pyroxene-bearing rocks (Adams, 1974). Consequently, other mineralogical phases such as olivine are easily inhibited, as already noted by Cloutis et al. (1986), Beck et al. (2013), and Carli et al. (2018), making their spectroscopic detection challenging. If olivine is present in relatively high amounts (>25%, Beck et al., 2013; Carli et al., 2018), the pyroxene absorption bands become wider and asymmetric, with the absorption band centers shifted toward longer wavelengths (Anbazhagan & Arivazhagan, 2009), a behavior that is not observed in Mare Ingenii. In fact, the lunar basalts are extremely rich in pyroxenes crystals rather than olivine (Papike et al., 1982; G. J. Taylor et al., 1991; Zhao et al., 2023).

One of the methods used for identifying olivine is the BAR value, which is nearly independent on particle sizes (Cloutis et al., 1986). As olivine lacks the band II absorption, low BAR values coupled with band I absorptions centered around 1.05 μm may suggest a substantial olivine abundance. The ratio between the two bands areas of Ingenii spectra (Figures 5k–5l) exhibits a quite narrow and high range of values (~1.32–1.76) likely indicating that olivine is not consistently abundant in the investigated area. Interestingly, dark material, swirl and intermediate regions show almost no variation in BAR values, related to mafic mineralogy (Figure 5k), but their BCI is definitely shifted toward longer values with respect to the BAR values. This indicates that BCI should be shifted for different reasons, possibly higher glass/melt abundances or strong weathering. On the other hand, bright material exhibits BAR values rather higher than other investigated areas, closer to the ol-opx line from Cloutis et al. (1986; Figure 5l), indicating a possible small variation in mafic composition (pyroxene compositions or pyroxenes/olivine variation) and a secondary effect related to other aspects such as size or roughness variations and space weathering.

Noteworthy, Ingenii basin material fall in a compositional field which does not identify in the range of values of the other maria of the SPA basin (e.g., Aitken, Leibnitz, Von Karman) recognized by X. Zhang et al. (2019) (Figure 5l). According to X. Zhang et al. (2019), the maria with the lowest BAR values are mainly located in the NW margin of the SPA basin, including Mare Ingenii (where authors indicate BAR values < 0.9). On the contrary, the highest BAR values are observed in the central and SE part of the basin, suggesting that the northern areas chiefly contain more olivine and/or Ca-pyroxene abundances (X. Zhang et al., 2019). In the present work, BAR values have been observed to be higher than 0.9 for the mare deposits (i.e., dark material ~1.4), so we can assert that olivine is likely not consistently abundant in the Ingenii basin.

Two interesting ROIs (i.e., ROI19 and ROI27) from small craters are characterized by distinctive features among all the bright material. ROI27 differs from the other spectra as it shows deeper absorption bands with respect to the overall trend. Moreover, it exhibits the highest absorption band area ratio (BAR = 1.74) among the explored bright materials, along with ROI18 (BAR = 1.66). Notably, ROI19 shows spectral features which are distinctly different from the adjacent ROI18, such as the lowest absorption band area ratio (BAR = 1.31), the highest FeO and TiO_2 amounts (~8.2 and ~1.0 wt%, respectively), and the highest global spectral slope (~0.66) among all the bright materials. Moreover, ROI19 absorption band centers values occur at relatively long wavelengths for

absorptions around 2 μm (BCII = 2.04 μm) but at moderately short wavelengths for band I (BCI = 0.91 μm), the latter likely appearing as suppressed. As mentioned above, low values of BAR (as observed for ROI19) are easily attributed to olivine occurrence, but this would hardly explain the suppression of band I, as the olivine phase only lacks band II. This clearly indicates that different processes affected the spectral features of the investigated area, and that some young small craters (i.e., bright material) appear fresher and less altered by space weathering. Indeed, Moon reflectance spectra are the result of several parameters, representing different mixtures of various mineralogical phases which underwent complex processes sometimes difficult to interpret. The investigated small craters are surrounded by heterogeneous terrains as the Moon's soil is strongly characterized by regolith and breccia fragments, which make any interpretation hard. The lunar surface appears to be extremely affected by space weathering, a process resulting from constant surface bombardments due to meteoric impacts, cosmic rays and solar wind which always characterize bodies lacking a substantial atmosphere (Noble & Pieters, 2003). Thus, mechanical and chemical alteration of the surface constantly contributes to the formation of agglutinates and iron nanophases (Fe^0) produced in the melt during the impact event (Noble et al., 2011; Pieters & Noble, 2016), which represent one of the main cause of alteration of spectral components (Hapke, 1973; Wehner, 1964), such as substantial reddening and darkening of the surface (Lucey & Riner, 2011; Pieters & Noble, 2016).

Anyway, laboratory spectra of mineral mixtures reveal that orthopyroxene is a very strong absorber and tends to dominate the spectra even if present in small amounts (~only 10–20 wt%, Horgan et al., 2014; Serventi et al., 2015). In contrast, the spectral contribution of plagioclase (the other mineralogical phase occurring in mare basalts, along with pyroxenes, olivine, and opaques) is unsubstantial and absorption bands do not show up if its contents is below 85% (X. Zhang & Cloutis, 2021a). Most of plagioclase varieties do not exhibit near-infrared absorption bands (Horgan et al., 2014) and rarely exhibit optical absorptions centered between 1.15 and 1.35 μm, as they are produced by electronic transitions of ferrous iron in its structure (Adams & Goullaud, 1978; Horgan et al., 2014; X. Zhang & Cloutis, 2021a), an element that has very low contents in plagioclase. Its absorption features are extremely weak, especially if compared to other iron-bearing phases (e.g., pyroxenes, Adams & Goullaud, 1978; Horgan et al., 2014). Moreover, masking of the Fe^{2+} plagioclase bands in rock spectra occurs when there are strong absorptions from ferrous iron in other minerals such as pyroxenes or olivine (Adams & Goullaud, 1978). Plagioclase occurrence then seems only to increase the albedo of a plagioclase-bearing lithology (Anbazhagan & Arivazhagan, 2009), even though space weathering is able to affect the spectral features of plagioclase, reducing significantly the absorption bands (Lucey et al., 2000; Yamamoto et al., 2015). Similarly, the spectral characteristics of ilmenite is rather complex and variable and its reflectance spectra result generally very dark. Ilmenite is substantially featureless in the VIS-NIR wavelengths (i.e., across the range of 0.3–2.5 μm, Izawa et al., 2021; Lemelin et al., 2013). However, it may show a broad absorption band at 0.5 μm (Adams, 1974; Adams & McCord, 1971), around 1.2 μm (Adams, 1974) or at 1.5 μm (Hunt et al., 1971) due to Fe-Ti crystal field transitions. Diagnostic spectral characteristics of ilmenite or other featureless phases are then not distinguishable, as their interpretation includes several factors, also because they can be considerably affected by particle sizes (Izawa et al., 2021). Moreover, ilmenite phase generally reduces the brightness and the absorption band depth in a rock mixture (Clark, 1983), so the spectral variations observed in Ingenii bright material might also be ascribed to small quantities of opaques in the small craters region.

4.2. Investigating the Swirl Region

Swirls are particular features found across the lunar surface, whose origin has not yet been fully clarified. They are defined as high-albedo sinuous morphologies and unraveling their formation mechanism certainly could help to provide some insights about geological processes occurring on the Moon's surface.

The most accredited hypothesis for their origin considers some local crustal magnetic anomalies which interact with the solar wind (Glotch et al., 2015; Hemingway & Garrick-Bethell, 2012; Hood & Coleman, 1979; Hood & Schubert, 1980; Kramer et al., 2011a, 2011b). Magnetometers on board the Apollo 15 and 16 missions mapped the lunar surface magnetic field (Hood, 1980; Hood & Schubert, 1980; Richmond & Hood, 2008; Richmond et al., 2005) and found that the largest magnetic anomalies match the brightest portions of the swirls (Blewett et al., 2011). Even though the Moon currently lacks an intrinsic magnetic field, these typical sinuous-shaped features might be ascribed to the orientation of fossil magnetic field remains (Denevi et al., 2016; Hemingway & Garrick-Bethell, 2012) that would be able to locally shield the surface from the space weathering by deflecting the solar wind (Halekas et al., 2009; Lue et al., 2011). For this reason, unraveling swirl formation mechanisms

and space environment effects on planetary surfaces is essential to understand the magnetic history of the Moon and to provide valuable constraints also about lunar soil migration and regolith transport (Domingue et al., 2022). Other hypotheses assume swirl origin as related to cometary impacts (e.g., Bruck Syal & Schultz, 2015; Schultz & Srnka, 1980), meteoroid swarms (e.g., Starukhina & Shkuratov, 2004) or refreshing of regolith and soil material from nearby crater ejecta (Blewett et al., 2011; Hood & Coleman, 1979).

In the Mare Ingenii region, Kramer et al. (2011a) recognized the highest value for magnetic field strength to match the swirl swarm occurring in the SW sector of the Thomson craters. Apparently, this is part of a more extensive swirls system widespread throughout the SPA basin (Denevi et al., 2016), yet Purucker et al. (2012) recognized a similar pattern in the geographic distribution of the magnetic anomalies only restricted to the NW corner of the SPA. A more in-depth investigation has been attempted by Purucker et al. (2012) regarding any possible correspondence of magnetic magnitude with the volume of lava deposits, but correlations appear weak or absent.

Spectral analysis conducted in this work on Mare Ingenii region have identified that the swirl located SW of Thomson craters (i.e., ROI 12–13) clearly show reflectance spectra (Figures 4c and 4d) which are clustered separately from the other swirl region, and show deeper absorption bands respect to the swirl located NE of Thomson crater (i.e., ROI 16–17). Moreover, ROI 12 shows spectral parameters which always deviate from the group average values (Figure 5), and this might represent different material or likely indicate that space weathering and other factors affected this ROI differently from other swirl regions. Indeed, ROI 13 is located in a marginal area of the Thomson M crater, whereas ROI 12 is in the inner region of the crater, overlying mare deposits. For this reason, the spectral behavior of this swirl region (i.e., ROI 12) could be easily affected by this type of material (e.g., abundance of low-Ca pyroxenes and Fe-rich phases could shift the absorption band centers toward longer wavelengths, as observed in this case; see Figures 5a, 5e, and 5f). Yet, it is worth noting that NE swirl regions (i.e., ROI 16–17) are also located in a comparable context as they superimpose mare deposits of the northern crater floor. For this reason, they should exhibit spectral features similar to ROI 12, but this is not observed. This confirms that the mineralogical component is not the primary factor controlling the spectral features.

FeO and TiO_2 abundances of the swirl areas exhibit values comparable to intermediate regions, which are slightly lower than maria deposits but higher than bright material. Indeed, most of the spectral parameters (such as the reflectance, band centers, BAR value and spectral slope) occupy a range of values which seems to be transitional between maria and bright deposits, likely suggesting mixed material between these two end-members. The global spectral slope helps in achieving a better understanding of the terrain maturity and the space weathering processes affecting the surface, and the different values of the investigated swirl regions (i.e., NE swirl = 0.75–0.77 and SW swirl = 0.56–0.67) suggest they are likely not coeval. The emplacement of these deposits probably did not occur at the same time, but it is tough to establish whether they are subsequent or not to the formation of the mare deposit. Indeed, if the swirl pattern was imprinted during the cooling lava, this would imply that an ancient dynamo may was active during the mare deposits emplacement.

It is thought that the SPA basin formation was a huge impact event, which might have led to a broad exposure of iron-rich material (Lucey et al., 1998). Thus, the study of magnetic lineaments might reveal aspects which can be related also to the emplacement of the Aitken basin itself and its ancient evolutionary history. The SPA basin is estimated to be formed between 4.2 and 4.3 Ga (i.e., Pre-Nectarian age; Ivanov et al., 2018) and as such it appears heavily degraded. The continuous meteoric bombardment would have surely obliterated the oldest lava plains and other surface geological features. For this reason, it still remains unclear the exact formation process and the timing of the emplacement of the SPA basin.

4.3. Geological Implication Within the Context of the SPA Basin

The SPA basin is heterogeneous in composition, showing anorthositic to noritic and gabbro-noritic compositions (Lemelin et al., 2019; Moriarty & Pieters, 2018; Tompkins & Pieters, 1999; X. Zhang et al., 2019). Indeed, SELENE/Kaguya Multiband Imager (MI) derived maps of mineral abundances revealing that the SPA spectral signature is clearly characterized by a mafic component (Jolliff et al., 2000; Lemelin et al., 2019; Yamamoto et al., 2023), chiefly ascribed to orthopyroxene occurrence compared to the neighboring areas (Moriarty & Pieters, 2018). Actually, four distinct compositional zones have been broadly identified by Moriarty and Pieters (2018) across the SPA basin. The identification was mainly based on compositional gradients of some

spectral features, specifically absorption band centers and band depths which have been evaluated with the attempt of recognizing the spatial distribution of the pyroxenes. Indeed, the central part of the basin seems to be dominated by the largest absorption depths and band centers, likely representing Ca- and Fe-rich pyroxenes (Moriarty & Pieters, 2018). These spectral parameters decrease toward the outer region (defined as Mg-pyroxenes annulus; Moriarty & Pieters, 2018) that is characterized by widespread Mg-rich pyroxenes (e.g., pigeonites and orthopyroxenes). Mare Ingenii is located in an outer region which is defined as a heterogeneous annulus by Moriarty and Pieters (2018), yet straddling the Mg-pyroxene ring border. This heterogeneous zone is roughly characterized by feldspathic material (which instead dominates the SPA exterior) with some localized Mg-pyroxenes in small central peaks (Moriarty & Pieters, 2018). These spectral characteristics cannot account for the emplacement and the mechanisms of formation of these minerals and lithologies. So, these elements cannot clarify whether these signatures are related to melting of crust-mantle boundary lithologies, impact melts or impact breccias as the spatial distribution of impact melts and excavated material still remains unknown (X. Zhang et al., 2019). However, such exposures of mafic minerals, especially of low-Ca and Ca-free pyroxenes, have been often interpreted as excavation of the lunar mantle (Lemelin et al., 2019; Lucey et al., 1998; Melosh et al., 2014; Miljkovic et al., 2013; Nakamura et al., 2012; Petro & Jolliff, 2013; Potter et al., 2012; Yamamoto et al., 2010). This hypothesis has been also suggested in order to account for olivine-rich exposures found in the central peaks of some regions (e.g., Schrödinger basin and Zeeman crater) or pyroxene-rich materials in some fresh craters (Yamamoto et al., 2012, 2023). Yet notably, by observing the Kaguya MI maps, the SPA basin is still dominated by a plagioclase-rich mineralogy (~55–65 wt%), even if at a lesser extent compared to the overall highlands distributions (~75–85 wt%). Plagioclase feldspar does represent an accessory phase (as well as the primary aluminum-bearing mineral) in the Earth's upper mantle, which results mainly composed of olivine and pyroxenes-rich rocks (i.e., peridotitic compositions). Thus, such small olivine-exposures in extremely localized areas of the SPA basin indicate that the ancient impact event did not necessarily involve excavation of lunar mantle. It might have rather revealed portions of the deeper lunar crust, since pure anorthositic compositions occur near the surface whereas more mafic compositions (e.g., norites, gabbros and troctolites) likely dominate the lower crust (i.e., around 5–10 km depth; Pieters, 1986; Pieters et al., 1997; Tompkins & Pieters, 1999). Indeed, they are not found in the central area of the SPA basin but rather as scattered points located on the outer rim, nor in the crater floors but along the peak rings (Yamamoto et al., 2012, 2023). This could validate the hypothesis for a certain local differentiation occurring in the melt layers during the SPA basin impact event, as suggested by Yamamoto et al. (2012). Subsequent impacts, responsible for the secondary craters (e.g., Schrödinger and Zeeman craters), would have then uplifted deep-seated materials (i.e., olivine-rich) in correspondence of their peak rings in the stratified crater floor (Yamamoto et al., 2012).

As previously mentioned, the Ingenii basin occurs in the outer region of the SPA terrain, where an average of ~5.7 wt% of FeO content has been detected by Jolliff et al. (2000) (different from the inner region where FeO is ~10 wt%). These relatively low iron abundances are chemically comparable to the ejecta areas of the feldspathic highlands terrains (Jolliff et al., 2000), and could then represent the deeper crust of the anorthositic covering which dominates the lunar farside (and almost ~80% of the entire lunar surface, Anbazhagan et al., 2021; Head, 1976; Pieters, 1986). Anorthositic crust is thought to be accumulated by plagioclase floatation after crystallization of the ancient magma ocean (Jolliff et al., 2000) and, along with Mg-rich rocks such as gabbros, norites, and troctolites, constitute the lower crust of the Moon (Anbazhagan et al., 2021; Jolliff et al., 2000).

Since it is assumed that the dominant rock type occurring throughout the SPA basin is likely norite, which better represents the mafic component of the lower crust (Pieters et al., 1997), reflectance spectra of some terrestrial gabbros and norites (Anbazhagan & Arivazhagan, 2011) have been then considered for a better qualitative comparison with Ingenii basin investigated spectra. Yet, most of the investigated ROIs in this work consist of mare materials, thus also spectra from some terrestrial basalts (Anbazhagan & Arivazhagan, 2009) have been evaluated as Mare Ingenii analogs. Despite the terrestrial rocks exhibit absorption features which typically recall the spectral features of pyroxene-rich phases (mostly resembling high-Ca pyroxene compositions, Anbazhagan & Arivazhagan, 2011), the Ingenii Basin's spectra barely resemble the terrestrial rocks characteristics. This is probably due to the relative differences of the bulk chemistry of the selected analogs which do not entirely match the lunar compositions (e.g., higher alkali and silica amounts and lower MgO contents) as their emplacements are far from geodynamical environments of the Moon.

However and noteworthy, some characteristics of Ingenii basin's bright materials could be comparable to the terrestrial gabbro-noritic spectral features. Indeed, most of the selected ROIs of the bright materials consist of

small craters which are actually located outside the mare material, being encompassed in the regional setting of the outer margin of the SPA basin, which is mainly constituted of ejecta and degraded rim deposits (Jolliff et al., 2000). Consequently, spectral signatures of the Ingenii bright materials might be ascribed to highlands breccias or other impact rocks (including several lithologies and various particle sizes) or maybe to some lithologies representing magmatic intrusions into the lower crust or rocks deriving from crust-mantle interface (Pieters et al., 2011).

4.3.1. Insights on Lunar TiO_2 Abundance Distribution

One important aspect to examine is the overall TiO_2 and ilmenite amount in the lunar basalts. Lunar basalts are highly reduced (S. R. Taylor & McLennan, 2009), and ferric iron is nearly absent. Ti-Fe-bearing opaque minerals are then represented by ilmenite or Fe-Ti-spinel (Neal & Taylor, 1992; Papike et al., 1998). Ilmenite is the major titanium carrier on the Moon and, for this reason, an improved knowledge of the spectral reflectance properties of ilmenites and other Fe-Ti oxides is needed to better understand lunar basalt source conditions and lunar interior compositions. Indeed, ilmenite formation depends on various parameters, mainly on the melt compositions as well as magma crystallization temperature, cooling rate, and oxygen fugacity. Then, it definitely represents a valuable petrogenetic indicator for unraveling the Moon mantle source evolution and could provide information about lunar magma ocean and its early historical evolution.

Sato et al. (2017) mapped TiO_2 abundances over some lunar maria, including Mare Ingenii. They identified some anomalies in the TiO_2 estimated content of some areas corresponding to the dark material of northern Thomson crater (more specifically, corresponding to ROIs 2-3-4-10-11 of the present study), showing much higher TiO_2 content (up to ∼7 wt%) than the one obtained in this work (i.e., max to ∼1.2 wt% with some areas showing TiO_2 content below the detection limit, namely <2 wt%). Such a high variation in a restricted area within a single mare might sound odd. Yet, Sato et al. (2017) estimations were derived from linear correlations between TiO_2 abundances of some Apollo soil returned samples and UVVIS reflectance observations derived from LROC-WAC global mosaic. For this reason, their TiO_2 abundances may be approximated to a rough estimate. Moreover, Apollo-returned samples show a bimodal distribution of TiO_2 abundances (G. J. Taylor et al., 1991) as most of the maria deposits show TiO_2 content up to ∼4 wt% (such as Mare Ingenii, defined as low-TiO_2 basalts, G. J. Taylor et al., 1991), whereas only 20% of the maria exhibits abundances >5 wt% (high-TiO_2 basalts, Giguere et al., 2000). Nevertheless, remote sensing analysis of nearside maria actually does not detect any compositional gap, but a continuum in titanium abundances (Giguere et al., 2000; Pieters, 1978). It is simply thought that the Apollo missions did not land in "intermediate" TiO_2 areas and those abundances were just not sampled.

Mare Moscoviense, another of the few maria occurring on the farside, exhibits higher TiO_2 contents (i.e., ∼4.5–7.5 wt%; Karthi et al., 2022) compared to Mare Ingenii, and for this reason its basaltic infill is thought to be generated from the melting of a mafic cumulate (i.e., olivine-pyroxene-ilmenite cumulate), likely originated as residual lower part of the stratified primordial crust formed during the magma ocean crystallization (Karthi et al., 2022). Furthermore, a general crustal thinning is usually observed below the maria basins, with Mare Moscoviense showing a crustal thickness <1 km (Wieczorek et al., 2012), in stark contrast to the crust of the farside which seems to exhibit a general thickness of ∼75 km (Wieczorek et al., 2012). Such a thick crust could certainly inhibit magma upwelling, preventing the emplacement of large basaltic plains on the surface, different from a thinner crust which instead would facilitate magma migration toward the surface. The thickness of the crust appears to be quite heterogeneous beneath Mare Ingenii, with ∼12–16 km in the central portion (i.e., in the western part of Thomson crater) up to ∼35–40 km toward the western outer margin of the basin. The exact thickness of the lunar crust is still quite unknown and several models have been proposed to explain the crustal dichotomy between the farside and the nearside of the Moon, but this asymmetry would easily explain the different mare basaltic distributions on the two lunar sides.

Several factors at different scales surely played important roles in the lunar surface processes. Yet, these applications have some limitations. On Earth, geological considerations are the result of samples collection, field surveys and in situ direct observations, whereas remote sensing data obtained by spacecraft usually must go through a processing chain (calibration, artifact removal, georeferentiation, photometric correction, etc.) that in most cases needs to be updated multiple times before allowing a reliable interpretation. Thus, a multidisciplinary approach is required for an efficient and extensive survey of the topic. Moreover, a direct geochemical and mineralogical analysis on the returned samples, together with geophysical data, could certainly provide more accurate constraints on the origin, differentiation, and evolution of the lunar rocks.

5. Concluding Remarks

Our spectroscopic analysis of Mare Ingenii reveals a mineralogical variability, mainly dominated by strong pyroxene absorptions. Dark material in Thomson craters' floors exhibits the absorption band center positions shifted to longer wavelengths (i.e., BCI = 0.96–0.99 μm and BCII = 2.03–2.12 μm), likely indicating the diagnostic spectral features of high-Ca pyroxenes (i.e., clinopyroxenes), similar to the swirl and intermediate albedo regions. FeO and TiO_2 abundances in this area are ∼10.6–11.4 and ∼1.1–1.2 wt%, respectively, supporting the hypothesis of an overall mafic component throughout the studied area (Jolliff et al., 2000; Lemelin et al., 2019). Conversely, the bright material of the small craters surrounding Mare Ingenii shows the lowest values for absorption band center positions (i.e., BCI = 0.91–0.94 μm and BCII = 1.91–2.04 μm), mostly resembling low-Ca clinopyroxenes or Ca-free pyroxenes, also exhibiting lower FeO and TiO_2 abundances (i.e., ∼5.0–8.2, ∼0.8–1.0 wt%, respectively). The BAR spectral parameter indicates that olivine is not abundant enough to be convincingly revealed in the Ingenii area, yet a broad range of higher values for the bright material suggests a variation in the mafic component or in the grain size or in the space weathering processes. Indeed, a general "blue" global spectral slope for the bright material may indicate fresh craters deposits. On the other hand, the swirl region shows variable values of spectral slope, likely supporting the hypothesis of more recent material with respect to the regional setting, yet showing a spectral behavior similar of the basaltic flood plains (i.e., chiefly dominated by high-Ca pyroxenes). Additionally, the swirl deposits seems to be similar to intermediate regions, as their spectral features recall mixed characteristics between dark and bright material.

Most of the mineralogical phases are difficult to detect via reflectance spectroscopy if Fe-bearing phases occur, such as pyroxene minerals whose spectral signatures tend to dominate the overall spectral profile even if present in small abundances (Horgan et al., 2014; Serventi et al., 2015). Several other variables complicate the interpretation of the mineralogy of an airless planetary body as inferred by reflectance spectroscopy. Moreover, lunar surface alteration and soil evolution are the consequence of space weathering effects, which usually involve spectral modifications. However, an overall mafic component seems to be widespread throughout the investigated area compared to nearby terrains (i.e., anorthositic highlands). Indeed, the Ingenii basin is located within the outer border of the SPA basin, the deepest and the oldest impact basin in our Solar System, which likely exposed the lower lunar crust. M^3 data suggest a strong contribution of the mafic component in the basin, with dominant pyroxene minerals (and local olivine-rich exposures; Yamamoto et al., 2012, 2023), likely representing the deeper section of the lunar crust dominated by gabbros, norites, and troctolites (Anbazhagan et al., 2021; Jolliff et al., 2000). Several hypotheses have been proposed to account for this mafic exposures, such as a huge collision that penetrated through the Moon's crust (Pieters et al., 1997; Yamamoto et al., 2012) or excavation of the mantle (Lemelin et al., 2019; Lucey et al., 1998; Melosh et al., 2014; Miljkovic et al., 2013; Nakamura et al., 2012; Petro & Jolliff, 2013; Potter et al., 2012; Yamamoto et al., 2010). Our mineralogical mapping is consistent with Mare Ingenii representing a lunar mare emplaced within a larger impact structure.

Mare Ingenii can be also considered a high-priority target for future robotic and human exploration for its pit. Indeed, pits are usually skylights into subsurface voids or caverns which might represent natural shelters against the space environment and so, in terms of exploration, they constitute ideal sites for human settlements, suitable for a better investigation of the lunar volcanic history and its geological evolution.

Anyway, while remote sensing is the easiest approach to perform mineralogical mapping of planetary bodies, including our Moon, a more detailed quantification of the mineralogical phases occurring on the Moon's surface, along with an in-depth study of the petrology of the returned samples and meteorites, is certainly required for a more comprehensive knowledge.

Data Availability Statement

The spectral parameter maps, the average spectra and the continuum removal spectra of the ROIs produced for this work are available in Zambon and Salari (2023). The high level maps shown in this paper are available at U.S. Geological Survey (USGS) Astrogeology Science Center (https://www.usgs.gov/centers/astrogeology-science-center). The LROC data sets are produced by the LROC Team at the Tempe campus of Arizona State University (PDS IMG, 2018). Lunar Orbiter Laser Altimeter (LOLA) data sets and KAGUYA Terrain Camera (TC) Digital Elevation Model (DEM) can be found in Smith et al. (2010) and Barker et al. (2016), respectively. The morpho-stratigraphic map was obtained using the ESRI software ArcGIS (https://www.arcgis.com/home/index.html) and the spectral analysis was processed by using the ENVI image analysis software (https://www.l3harrisgeospatial.com).

Acknowledgments
We acknowledge support from the PRIN INAF (RIC) 2019 project: "MELODY: Moon multisEnsor and LabOratory Data analYsis," selected by the Scientific Directorate of Italy's National Institute for Astrophysics (INAF) on 10 November 2020 and funded with 167,162 euros (INAF Grant 1.05.01.85.17). The authors thank one anonymous referee and Satoru Yamamoto for their valuable comments that greatly improved the quality of this manuscript.

References

Adams, J. B. (1974). Visible and near-infrared diffuse reflectance spectra of pyroxenes as applied to remote sensing of solid objects in the solar system. *Journal of Geophysical Research*, *79*(32), 4829–4836. https://doi.org/10.1029/jb079i032p04829

Adams, J. B. (1975). Interpretation of visible and near-infrared diffuse reflectance spectra of pyroxenes and other rock forming minerals. In C. Karr (Ed.), *Infrared and Raman spectroscopy of lunar and terrestrial materials* (pp. 91–116). Academic Press.

Adams, J. B., & Goullaud, L. H. (1978). Plagioclase feldspars - Visible and near infrared diffuse reflectance spectra as applied to remote sensing. In *Lunar and Planetary Science Conference Proceedings* (Vol. 9, pp. 2901–2909).

Adams, J. B., & McCord, T. B. (1971). Optical properties of mineral separates, glass, and anorthositic fragments from Apollo mare samples. In *Lunar and Planetary Science Conference Proceedings* (Vol. 2, pp. 2183–2195).

Anbazhagan, S., & Arivazhagan, S. (2009). Reflectance spectra of analog basalts; implications for remote sensing of lunar geology. *Planetary and Space Science*, *57*(12), 1346–1358. https://doi.org/10.1016/j.pss.2009.06.020

Anbazhagan, S., & Arivazhagan, S. (2011). Characterization of reflectance spectra of lunar analog rocks: Gabbro and norite. *Current Science*, *100*, 761–768.

Anbazhagan, S., Venugopal, I., Arivazhagan, E., Chinnamuthu, M., Paramasivam, C. R., Nagesh, G., et al. (2021). A lunar soil simulant (LSS-ISAC-1) for the lunar exploration programme of the Indian Space Research Organisation. *Icarus*, *366*, 114511. https://doi.org/10.1016/j.icarus.2021.114511

Barker, M. K., Mazarico, E., Neumann, G. A., Zuber, M. T., Haruyama, J., & Smith, D. E. (2016). A new lunar digital elevation model from the lunar orbiter laser altimeter and SELENE terrain camera. *Icarus*, *273*, 346–355. https://doi.org/10.1016/j.icarus.2015.07.039

Beck, A. W., McCoy, T. J., Sunshine, J. M., Viviano, C. E., Corrigano, C. M., Hiroi, T., & Mayne, R. G. (2013). Challenges in detecting olivine on the surface of 4 Vesta. *Meteoritics & Planetary Sciences*, *48*(11), 2155–2165. https://doi.org/10.1111/maps.12160

Besse, S., Sunshine, J., Staid, M., Boardman, J., Pieters, C., Guasqui, P., et al. (2013a). A visible and near-infrared photometric correction for Moon Mineralogy Mapper (M^3). *Icarus*, *222*(1), 229–242. https://doi.org/10.1016/j.icarus.2012.10.036

Besse, S., Yokota, Y., Boardman, J., Green, R., Haruyama, J., Isaacson, P., et al. (2013b). One Moon, many measurements 2: Photometric corrections. *Icarus*, *226*(1), 127–139. https://doi.org/10.1016/j.icarus.2013.05.009

Blewett, D. T., Coman, E. I., Hawke, B. R., Gillis-Davis, J. J., Purucker, M. E., & Hughes, C. G. (2011). Lunar swirls: Examining crustal magnetic anomalies and space weathering trends. *Journal of Geophysical Research*, *116*(E2), E02002. https://doi.org/10.1029/2010JE003656

Bruck Syal, M., & Schultz, P. H. (2015). Cometary impact effects at the Moon: Implications for lunar swirl formation. *Icarus*, *257*, 194–206. https://doi.org/10.1016/j.icarus.2015.05.005

Burns, R. G. (1970). *Mineralogical applications of crystal field theory* (p. 224). Cambridge University Press. https://doi.org/10.1017/CBO9780511524899

Burns, R. G. (1993). *Mineralogical applications of crystal field theory* (2nd ed., p. 551). Cambridge University Press.

Carli, C., Pratesi, G., Moggi-Cecchi, V., Zambon, F., Capaccioni, F., & Santoro, S. (2018). Northwest Africa 6232: Visible–near infrared reflectance spectra variability of an olivine diogenite. *Meteoritics & Planetary Sciences*, *53*(10), 2228–2242. https://doi.org/10.1111/maps.13056

Clark, R. N. (1983). Spectral properties of mixtures of Montmorillonite and dark carbon grains: Implications for remote sensing minerals containing chemically and physically adsorbed water. *Journal of Geophysical Research*, *88*(B12), 10635–10644. https://doi.org/10.1029/JB088iB12p10635

Clark, R. N. (1999). Spectroscopy of rocks and minerals and principles of spectroscopy. In A. N. Rencz (Ed.), *Manual of remote sensing* (Vol. 3, pp. 3–58). John Wiley & Sons.

Clark, R. N., & Roush, T. L. (1984). Reflectance spectroscopy: Quantitative analysis techniques for remote sensing applications. *Journal of Geophysical Research*, *89*(B7), 6329–6340. https://doi.org/10.1029/JB089iB07p06329

Cloutis, E. A. (2002). Pyroxene reflectance spectra: Minor absorption bands and effects of elemental substitutions. *Journal of Geophysical Research*, *107*(E6), E65039. https://doi.org/10.1029/2001JE001590

Cloutis, E. A., Gaffey, M. J., Jackowski, T. L., & Reed, K. L. (1986). Calibrations of phase abundance, composition, and particle size distribution for olivine-orthopyroxene mixtures from reflectance spectra. *Journal of Geophysical Research*, *91*(B11), 11641–11653. https://doi.org/10.1029/JB091iB11p11641

Cloutis, E. A., Sunshine, J. M., & Morris, R. V. (2004). Spectral reflectance-compositional properties of spinels and chromites: Implications for planetary remote sensing and geothermometry. *Meteoritics & Planetary Sciences*, *39*(4), 545–565. https://doi.org/10.1111/j.1945-5100.2004.tb00918.x

Cuzzi, J., Clark, R., Filacchione, G., French, R., Johnson, R., Marouf, E., et al. (2009). Ring particle composition and size distribution. In M. K. Dougherty, L. W. Esposito, & S. M. Krimigis (Eds.), *Saturn from cassini-huygens*. Springer. https://doi.org/10.1007/978-1-4020-9217-6_15

Denevi, B. W., Lucey, P. G., Hockberg, E. J., & Steutel, D. (2007). Near-infrared optical constants of pyroxene as a function of iron and calcium content. *Journal of Geophysical Research*, *112*(E5), E05009. https://doi.org/10.1029/2006JE002802

Denevi, B. W., Robinson, M. S., Boyd, A. K., Blewett, D. T., & Klima, R. L. (2016). The distribution and extent of lunar swirls. *Icarus*, *273*, 53–67. https://doi.org/10.1016/j.icarus.2016.01.017

Domingue, D., Weirich, J., Chuang, F., Sickafoose, A., & Palmer, E. (2022). Topographic correlations within lunar swirls in mare Ingenii. *Geophysical Research Letters*, *49*(6), e2021GL095285. https://doi.org/10.1029/2021GL095285

Farcy, B., Arevalo, R. J., & McDonough, F. (2021). Understanding the lunar nearside–farside dichotomy via in situ trace element measurements: The scientific framework of a prospective landed mission. *The Planetary Science Journal*, *2*, 80. https://doi.org/10.3847/PSJ/abee7f

Filacchione, G., Capaccioni, F., Ciarniello, M., Clark, R. N., Cuzzi, J. N., Nicholson, P. D., et al. (2012). Saturn's icy satellites and rings investigated by Cassini-VIMS: III-radial compositional variability. *Icarus*, *320*(2), 1064–1096. https://doi.org/10.1016/j.icarus.2012.06.040

Fortezzo, C. M., Spudis, P. D., & Harrel, S. L. (2020). Release of the digital unified global geologic map of the moon at 1:5,000,000-scale. In *51st lunar and planetary science conference* (No. (2760)). Retrieved from https://www.hou.usra.edu/meetings/lpsc2020/pdf/2760.pdf

Gaffey, M. J. (1976). Spectral reflectance characteristics of the meteorite classes. *Journal of Geophysical Research*, *81*(5), 905–920. https://doi.org/10.1029/JB081i005p00905

Gaffey, M. J., Bell, J. F., Brown, R. H., Burbine, T. H., Piatek, J. L., Reed, K. L., & Chaky, D. A. (1993). Mineralogical variations within the S-type asteroid class. *Icarus*, *106*(2), 573–602. https://doi.org/10.1006/icar.1993.1194

Garrick-Bethell, I., Head, J. W., & Pieters, C. M. (2011). Spectral properties, magnetic fields, and dust transport at lunar swirls. *Icarus*, *212*(2), 480–492. https://doi.org/10.1016/j.icarus.2010.11.036

Garrick-Bethell, I., Nimmo, F., & Wieczorek, M. A. (2010). Structure and formation of the lunar farside highlands. *Science*, *330*(6006), 949–951. https://doi.org/10.1126/science.1193424

Giguere, T. A., Taylor, G. J., Hawke, B. R., & Lucey, P. G. (2000). The titanium contents of lunar mare basalts. *Meteoritics & Planetary Sciences*, *35*(1), 193–200. https://doi.org/10.1111/j.1945-5100.2000.tb01985.x

Glotch, T., Bandfield, J., Lucey, P., Hayne, P. O., Greenhagen, B. T., Arnold, J. A., et al. (2015). Formation of lunar swirls by magnetic field standoff of the solar wind. *Nature Communications*, *6*(1), 6189. https://doi.org/10.1038/ncomms7189

Green, R. O., Pieters, C., Mouroulis, P., Eastwood, M., Boardman, J., Glavich, T., et al. (2011). The Moon Mineralogy Mapper (M^3) imaging spectrometer for lunar science: Instrument description, calibration, on-orbit measurements, science data calibration and on-orbit validation. *Journal of Geophysical Research*, *116*, E10. https://doi.org/10.1029/2011JE003797

Gross, J., Hilton, A., Prissel, T. C., Setera, J. B., Korotev, R. L., & Calzada-Diaz, A. (2020). Geochemistry and petrogenesis of Northwest Africa 10401: A new type of the Mg-suite rocks. *Journal of Geophysical Research: Planets*, *125*(5), e2019JE006225. https://doi.org/10.1029/2019JE006225

Halekas, J. S., Delory, G. T., Lin, R. P., Stubbs, T. J., & Farrell, W. M. (2009). Lunar surface charging during solar energetic particle events: Measurement and prediction. *Journal of Geophysical Research*, *114*(A5), A05110. https://doi.org/10.1029/2009JA014113

Hapke, B. W. (1973). Darkening of silicate rock powders by solar wind sputtering. *The Moon*, *7*(3–4), 342–355. https://doi.org/10.1007/BF00564639

Haruyama, J., Hara, S., Hioki, K., Morota, T., Yokota, Y., Shirao, M., et al. (2010). New discoveries of lunar holes in mare Tranquillitatis and mare Ingenii. In *41st lunar and planetary science conference* (No. (1533)).

Haruyama, J., Hioki, K., Shirao, M., Morota, T., Hiesinger, H., Van der Bogert, C., et al. (2009). Possible lunar lava tube skylight observed by SELENE cameras. *Geophysical Research Letters*, *36*(21), L21206. https://doi.org/10.1029/2009GL040635

Head, J. W. (1976). Lunar volcanism in space and time. *Reviews of Geophysics*, *14*(2), 265–300. https://doi.org/10.1029/RG014i002p00265

Hemingway, D. J., & Garrick-Bethell, I. (2012). Magnetic field direction and lunar swirl morphology: Insights from Airy and Reiner Gamma. *Journal of Geophysical Research*, *117*(E10), E10012. https://doi.org/10.1029/2012JE004165

Hood, L. L. (1980). Bulk magnetization properties of the Fra Mauro and Reiner Gamma formations. In *Proceedings of the Lunar Science Conference* (Vol. 3, pp. 1879–1896).

Hood, L. L., & Coleman, P. J. (1979). Lunar nearside magnetic anomalies. In *Proceedings of the Lunar and Planetary Science Conference* (Vol. 3, pp. 2235–2257). https://doi.org/10.1126/science.208.4439.4

Hood, L. L., & Schubert, G. (1980). Lunar magnetic anomalies and surface optical properties. *Science*, *208*(4439), 49–51. https://doi.org/10.1126/science.208.4439.49

Hood, L. L., Zakharian, A., Halekas, J., Mitchell, D., Lin, R., Acuña, M. H., & Binder, A. B. (2001). Initial mapping and interpretation of lunar crustal magnetic anomalies using Lunar prospector magnetometer data. *Journal of Geophysical Research*, *106*(E11), 27825–27839. https://doi.org/10.1029/2000JE001366

Horgan, B. H. N., Cloutis, E. A., Mann, P., & Bell, J. F. (2014). Near-infrared spectra of ferrous mineral mixtures and methods for their identification in planetary surface spectra. *Icarus*, *234*, 132–154. https://doi.org/10.1016/j.icarus.2014.02.031

Hunt, G. R., Salisbury, J. W., & Lenhoff, C. J. (1971). Visible and near infrared spectra of minerals and rocks: III. Oxides and hydroxides. *Modern Geology*, *2*, 195–205.

Ivanov, M. A., Hiesinger, H., van der Bogert, C. H., Orgel, C., Pasckert, J. H., & Head, J. W. (2018). Geologic history of the northern portion of the South Pole-Aitken basin on the Moon. *Journal of Geophysical Research: Planets*, *123*(10), 2585–2612. https://doi.org/10.1029/2018JE005590

Izawa, M. R. M., Applin, D. M., Morison, M. Q., Cloutis, E. A., Mann, P., & Mertzman, S. A. (2021). Reflectance spectroscopy of ilmenites and related Ti and Ti single bond Fe oxides (200 to 2500 nm): Spectral-compositional-structural relationships. *Icarus*, *362*, 114423. https://doi.org/10.1016/j.icarus.2021.114423

Ji, J., Guo, D., Liu, J., Chen, S., Ling, Z., Ding, X., Et al. (2022). The 1:2,500,000-scale geologic map of the global Moon. *Science Bulletin*, *67*(15), 1544–1548. https://doi.org/10.1016/j.scib.2022.05.021

Jolliff, B. L., Gillis, J. J., Haskin, L. A., Korotev, R. L., & Wieczorek, M. (2000). Major lunar crustal terranes: Surface expressions and crust-mantle origins. *Journal of Geophysical Research*, *105*(E2), 4197–4216. https://doi.org/10.1029/1999JE001103

Jutzi, M., & Asphaug, E. (2011). Forming the lunar farside highlands by accretion of a companion moon. *Nature*, *476*(7358), 69–72. https://doi.org/10.1038/nature10289

Karthi, A., Arivazhagan, S., & Sharma, M. (2022). Mapping of compositional diversity and chronological ages of lunar farside multiring mare Moscoviense basin: Implications to the middle Imbrian mare basalts. *Research in Astronomy and Astrophysics*, *22*(12), 125002. https://doi.org/10.1088/1674-4527/ac8f8c

King, T. V. V., & Ridley, W. I. (1987). Relation of the spectroscopic reflectance of olivine to mineral chemistry and some remote sensing implications. *Journal of Geophysical Research*, *92*(B11), 11457–11469. https://doi.org/10.1029/JB092iB11p11457

Klima, R. L., Dyar, D. M., & Pieters, C. M. (2011). Near-infrared spectra of clinopyroxenes: Effects of calcium content and crystal structure. *Meteoritics & Planetary Sciences*, *46*(3), 379–395. https://doi.org/10.1111/j.1945-5100.2010.01158.x

Klima, R. L., Pieters, C. M., & Dyar, M. D. (2007). Spectroscopy of synthetic Mg-Fe pyroxenes I: Spin-allowed and spin-forbidden crystal field bands in the visible and near-infrared. *Meteoritics & Planetary Sciences*, *42*(2), 235–253. https://doi.org/10.1111/j.1945-5100.2007.tb00230.x

Korotev, R. L., Jolliff, B. L., Zeigler, R. A., Gillis, J. J., & Haskin, L. A. (2003). Feldspathic lunar meteorites and their implications for compositional remote sensing of the lunar surface and the composition of the lunar crust. *Geochimica et Cosmochimica Acta*, *67*(24), 4895–4923. https://doi.org/10.1016/j.gca.2003.08.001

Kramer, G. Y., Besse, S., Dhingra, D., Nettles, J., Klima, R., Garrick-Bethell, I., et al. (2011a). M^3 spectral analysis of lunar swirls and the link between optical maturation and surface hydroxyl formation at magnetic anomalies. *Journal of Geophysical Research*, *116*(E9), E00G18. https://doi.org/10.1029/2010JE003729

Kramer, G. Y., Combe, J.-P., Harnett, E. M., Hawke, B. R., Noble, S. K., Blewett, D. T., et al. (2011b). Characterization of lunar swirls at mare Ingenii: A model for space weathering at magnetic anomalies. *Journal of Geophysical Research*, *116*(E4), E04008. https://doi.org/10.1029/2010JE003669

Lemelin, M., Lucey, P. G., Miljkovic, K., Gaddis, L. R., Hare, T., & Ohtake, M. (2019). The compositions of the lunar crust and upper mantle: Spectral analysis of the inner rings of lunar impact basins. *Planetary and Space Science*, *165*, 230–243. https://doi.org/10.1016/j.pss.2018.10.003

Lemelin, M., Morisset, C. E., Germain, M., Hipkin, V., Goïta, K., & Lucey, P. G. (2013). Ilmenite mapping of the lunar regolith over Mare Australe and Mare Ingenii regions: An optimized multisource approach based on Hapke radiative transfer theory. *Journal of Geophysical Research: Planets*, *118*(12), 2582–2593. https://doi.org/10.1002/2013JE004392

Lucey, P. G., Blewett, D. T., & Jolliff, B. L. (2000). Lunar iron and titanium abundance algorithms based on final processing of Clementine ultraviolet-visible images. *Journal of Geophysical Research*, *105*(E8), 20297–20305. https://doi.org/10.1029/1999JE001117

Lucey, P. G., & Riner, M. A. (2011). The optical effects of small iron particles that darken but do not redden: Evidence of intense space weathering on Mercury. *Icarus*, *212*(2), 451–462. https://doi.org/10.1016/j.icarus.2011.01.022

Lucey, P. G., Taylor, G. J., Hawke, B. R., & Spudis, P. D. (1998). FeO and TiO_2 concentrations in the South Pole-Aitken basin - implications for mantle composition and basin formation. *Journal of Geophysical Research*, *103*(E2), 3701–3708. https://doi.org/10.1029/97JE03146

Lue, C., Futaana, Y., Barabash, S., Wiser, M., Holmström, M., Bhardwaj, A., et al. (2011). Strong influence of lunar crustal fields on the solar wind flow. *Geophysical Research Letters: Planets*, *38*(3), L03202. https://doi.org/10.1029/2010GL046215

McEwen, A. S., & Robinson, M. S. (1997). Mapping the moon by clementine. *Advances in Space Research*, *19*(10), 1523–1533. https://doi.org/10.1016/S0273-1177(97)00365-7

Melosh, H. J., Kendall, J., Johnson, B. C., Bowling, T., & Horgan, B. (2014). The Moon's upper mantle: Mostly OPX, not olivine? In *45th proceedings of the lunar and planetary science conference* (No. (2505)).

Miljkovic, K., Wieczorek, M. A., Collins, G. S., Laneuville, M., Neumann, G. A., Melosh, H. J., et al. (2013). Asymmetric distribution of lunar impact basins caused by variations in target properties. *Science*, *342*(6159), 724–726. https://doi.org/10.1126/science.1243224

Moriarty, D. P., III, & Pieters, C. M. (2018). The character of South Pole-Aitken Basin: Patterns of surface and subsurface composition. *Journal of Geophysical Research: Planets*, *123*(3), 729–747. https://doi.org/10.1002/2017JE005364

Nagaoka, H., Karouji, Y., Arai, T., Ebihara, M., & Hasebe, N. (2013). Geochemistry and mineralogy of a feldspathic lunar meteorite (regolith breccia), Northwest Africa 2200. *Polar Science*, *7*(3–4), 241–259. https://doi.org/10.1016/j.polar.2013.09.001

Nakamura, R., Yamamoto, S., Matsunaga, T., Ishihara, Y., Morota, T., Hiroi, T., et al. (2012). Compositional evidence for an impact origin of the Moon's Procellarum basin. *Nature Geoscience*, *5*(11), 775–778. https://doi.org/10.1038/ngeo1614

Neal, C. R., & Taylor, L. A. (1992). Petrogenesis of mare basalts: A record of lunar volcanism. *Geochimica et Cosmochimica Acta*, *56*(6), 2177–2211. https://doi.org/10.1016/0016-7037(92)90184-K

Noble, S. K., Hiroi, T., Keller, L. P., Rahman, Z., Sasaki, S., & Pieters, C. M. (2011). Experimental space weathering of ordinary chondrites by nanopulse laser: TEM results. In *42nd lunar and planetary science conference* (No. (1382)).

Noble, S. K., & Pieters, C. M. (2003). Space weathering on Mercury: Implications for remote sensing. *Solar System Research*, *37*(1), 31–35. https://doi.org/10.1023/A:1022395605024

Ohtake, M., Takeda, H., Matsunaga, T., Yokota, Y., Haruyama, J., Morota, T., et al. (2012). Asymmetric crustal growth on the Moon indicated by primitive farside highland materials. *Nature Geoscience*, *5*(6), 384–388. https://doi.org/10.1038/ngeo1458

Papike, J. J., Ryder, G., & Shearer, C. K. (1998). Lunar samples. *Reviews in Mineralogy and Geochemistry*, *36*, 5-1–5-234.

Papike, J. J., Simon, S. B., & Laul, J. C. (1982). The lunar regolith: Chemistry, mineralogy, and petrology. *Reviews of Geophysics and Space Physics*, *20*(4), 761–826. https://doi.org/10.1029/rg020i004p00761

Petro, E. N., & Jolliff, B. L. (2013). Thin crust in the South Pole-Aitken basin and samples from the mantle? Implications for south Pole-Aitken basin sampling in light of recent GRAIL results. In *44th lunar and planetary science conference* (No. (2724)).

Pieters, C. M. (1978). Mare basalt types on the front side of the moon: A summary of spectral reflectance data. In *Lunar and Planetary Science Conference* (Vol. 3, pp. 2825–2849).

Pieters, C. M. (1986). Composition of the lunar highland crust from near-infrared spectroscopy. *Reviews of Geophysics*, *24*(3), 557–578. https://doi.org/10.1029/rg024i003p00557

Pieters, C. M., Ammannito, E., Blewett, D. T., Denevi, B. W., De Sanctis, M. C., Gaffey, M. J., et al. (2012). Distinctive space weathering on Vesta from regolith mixing processes. *Nature*, *491*(7422), 79–82. https://doi.org/10.1038/nature11534

Pieters, C. M., Boardman, J., Buratti, B., Chatterjee, A., Clark, R., Glavich, T., et al. (2009). The moon mineralogy mapper (M^3) on Chandrayaan-1. *Current Science*, *96*, 500–505.

Pieters, C. M., Head, J. W., Dhingra, D., Isaacson, P., Klima, R., Petro, N., et al. (2011). Composition of the lower crust identified at basin rings. *EPSC Abstracts*, *6*. EPSC-DPS2011-1142-2.

Pieters, C. M., & Noble, S. K. (2016). Space weathering on airless bodies. *Journal of Geophysical Research: Planets*, *121*(10), 1865–1884. https://doi.org/10.1002/2016JE005128

Pieters, C. M., Tompkins, S., Head, J., & Hess, P. C. (1997). Mineralogy of the mafic anomaly in the South Pole-Aitken basin: Implications for excavation of the lunar mantle. *Geophysical Research Letters*, *24*(15), 1903–1906. https://doi.org/10.1029/97GL01718

Pinet, P. C., Shevchenko, V. V., Chevrel, S. D., Daydou, Y., & Rosemberg, C. (2000). Local and regional lunar regolith characteristics at Reiner Gamma formation: Optical and spectroscopic properties from Clementine and Earth-based data. *Journal of Geophysical Research*, *105*(E4), 9457–9475. https://doi.org/10.1029/1999JE001086

Planetary Data Systems (PDS) Cartography and Imaging Sciences (IMG). (2018). Lunar reconnaissance orbiter. Retrieved from https://pds-imaging.jpl.nasa.gov/portal/lro_mission.html

Potter, R. W. K., Collins, G. S., Kiefer, W. S., McGovern, P. J., & Kring, D. A. (2012). Constraining the size of the South Pole-Aitken basin impact. *Icarus*, *220*(2), 730–743. https://doi.org/10.1016/j.icarus.2012.05.032

Purucker, M. E., Head, J. W., & Wilson, L. (2012). Magnetic signature of the lunar South Pole-Aitken basin: Character, origin, and age. *Journal of Geophysical Research*, *117*(E5), E05001. https://doi.org/10.1029/2011JE003922

Richmond, N. C., & Hood, L. L. (2008). A preliminary global map of the vector lunar crustal magnetic field based on Lunar Prospector magnetometer data. *Journal of Geophysical Research*, *113*(E2), E02010. https://doi.org/10.1029/2007JE002933

Richmond, N. C., Hood, L. L., Mitchell, D. L., Lin, R. P., Acuña, M. H., & Binder, A. B. (2005). Correlations between magnetic anomalies and surface geology antipodal to lunar impact basins. *Journal of Geophysical Research*, *110*(E5), E05011. https://doi.org/10.1029/2005JE002405

Robinson, M. S., Brylow, S. M., Humm, D., Lawrence, S. J., Thomas, P. C., Denevi, B. W., et al. (2010). Lunar reconnaissance orbiter camera (LROC) instrument overview. *Space Science Reviews*, *150*(1–4), 81–124. https://doi.org/10.1007/s11214-010-9634-2

Rosenbush, V. K. (2005). Opposition effects in brightness, color, and polarization of comet 1P/Halley: Comparison with atmosphereless solar system bodies. *Solar System Research*, *39*(4), 312–321. https://doi.org/10.1007/s11208-005-0045-y

Roy, A., Wright, J. T., & Sigurðsson, S. (2014). Earthshine on a young moon: Explaining the lunar farside highlands. *The Astrophysical Journal Letters*, *788*(2), L42. https://doi.org/10.1088/2041-8205/788/2/L42

Sato, H., Robinson, M. S., Laurence, S. J., Denevi, B. W., Hapke, B., Jolliff, B. L., & Hiesenger, H. (2017). Lunar mare TiO_2 abundances estimated from UV/Vis reflectance. *Icarus*, *296*, 216–238. https://doi.org/10.1016/j.icarus.2017.06.013

Schultz, P. H., & Srnka, L. J. (1980). Cometary collisions on the moon and Mercury. *Nature*, *284*(5751), 22–26. https://doi.org/10.1038/284022a0

Serventi, G., Carli, C., & Sgavetti, M. (2015). Spectral variability of plagioclase–mafic mixtures (3): Quantitative analysis applying the MGM algorithm. *Icarus*, *254*, 34–55. https://doi.org/10.1016/j.icarus.2015.03.024

Serventi, G., Carli, C., Sgavetti, M., Ciarniello, M., Capaccioni, F., & Pedrazzi, G. (2013). Spectral variability of plagioclase–mafic mixtures (1): Effects of chemistry and modal abundance in reflectance spectra of rocks and mineral mixtures. *Icarus*, *226*(1), 282–298. https://doi.org/10.1016/j.icarus.2013.05.041

Shearer, C. K., Elardo, S. M., Petro, N. E., Borg, L. E., & McCubbin, F. M. (2015). Origin of the lunar highlands Mg-suite: An integrated petrology, geochemistry, chronology, and remote sensing perspective. *American Mineralogist*, *100*(1), 294–325. https://doi.org/10.2138/am-2015-4817

Shkuratov, Y., Starukhina, L., Hoffmann, H., & Arnold, G. (1999). A model of spectral albedo of particulate surfaces: Implications for optical properties of the moon. *Icarus*, *137*(2), 235–246. https://doi.org/10.1006/icar.1998.6035

Smith, D. E., Zuber, M. T., Neumann, G. A., Lemoine, F. G., Mazarico, E., Torrence, M. H., et al. (2010). Initial observations from the lunar orbiter laser altimeter (LOLA). *Geophysical Research Letters*, *37*(18), L18204. https://doi.org/10.1029/2010GL043751

Spudis, P. D., Reisse, R. A., & Gillis, J. J. (1994). Ancient multiring basins on the Moon revealed by Clementine laser altimetry. *Science*, *266*(5192), 1848–1851. https://doi.org/10.1126/science.266.5192.1848

Starukhina, L. V., & Shkuratov, Y. G. (2004). Swirls on the moon and Mercury: Meteoroid swarm encounters as a formation mechanism. *Icarus*, *167*(1), 136–147. https://doi.org/10.1016/j.icarus.2003.08.022

Sun, Z., Lv, Y., & Tong, Z. (2016). Effects of particle size on bidirectional reflectance factor measurements from particulate surfaces. *Optics Express*, *24*(6), A612–A634. https://doi.org/10.1364/OE.24.00A612

Sunshine, J. M., & Pieters, C. M. (1998). Determining the composition of olivine from reflectance spectroscopy. *Journal of Geophysical Research*, *103*(E6), 13675–13688. https://doi.org/10.1029/98JE01217

Taylor, G. J., Warren, P. H., Ryder, G., Delano, J., Pieters, C. M., & Lofgren, G. (1991). Lunar rocks. In G. H. Heiken, D. T. Vaniman, & B. M. French (Eds.), *Lunar sourcebook* (pp. 183–284). Cambridge University Press.

Taylor, S. R., & McLennan, S. (2009). Planetary crusts: Their composition, origin and evolution. In *Cambridge planetary science* (Vol. 10). Cambridge University Press.

Tompkins, S., & Pieters, C. M. (1999). Mineralogy of the lunar crust: Results from Clementine. *Meteoritics & Planetary Sciences*, *34*(1), 25–41. https://doi.org/10.1111/j.1945-5100.1999.tb01729.x

Wehner, G. K. (1964). In J. W. Salisbury & P. E. Glaser (Eds.), *The lunar surface layer* (pp. 313–322). Academic Press.

Wieczorek, M. A., Neumann, G. A., Nimmo, F., Kiefer, W. S., Taylor, G. J., Melosh, H. J., et al. (2012). The crust of the Moon as seen by GRAIL. *Science*, *339*(6120), 671–675. https://doi.org/10.1126/science.1231530

Wilhelms, D. E., Howard, K. A., & Wilshire, H. G. (1979). Geologic map of the South side of the moon, scale 1:5,000,000 (p. I-1162). U.S. Geol. Surv. Miscell. Invest. Ser.

Wilhelms, D. E., McCauley, J. F., & Trask, N. J. (1987). The geologic history of the Moon (p. 1348). USGS Professional Paper. https://doi.org/10.3133/pp1348

Yamamoto, S., Nagaoka, H., Ohtake, M., Kayama, M., Karouji, Y., Ishihara, Y., & Haruyama, J. (2023). Lunar mantle composition based on spectral and geologic analysis of low-Ca pyroxene and olivine-rich rocks exposed on the lunar surface. *Journal of Geophysical Research: Planets*, *128*(5), e2023JE007817. https://doi.org/10.1029/2023JE007817

Yamamoto, S., Nakamura, R., Matsunaga, T., Ogawa, Y., Ishihara, Y., Morota, T., et al. (2010). Possible mantle origin of olivine around lunar impact basins detected by SELENE. *Nature Geoscience*, *3*(8), 533–536. https://doi.org/10.1038/ngeo897

Yamamoto, S., Nakamura, R., Matsunaga, T., Ogawa, Y., Ishihara, Y., Morota, T., et al. (2012). Olivine-rich exposures in the South Pole-Aitken basin. *Icarus*, *218*(1), 331–344. https://doi.org/10.1016/j.icarus.2011.12.012

Yamamoto, S., Nakamura, R., Matsunaga, T., Ogawa, Y., Ishihara, Y., Morota, T., et al. (2015). Featureless spectra on the Moon as evidence of residual lunar primordial crust. *Journal of Geophysical Research: Planets*, *120*(12), 2190–2205. https://doi.org/10.1002/2015/JE004935

Zambon, F., & Salari, G. (2023). Mare Ingenii regions of interest spectra continuum removal from Salari et al. 2023 [Dataset]. Zenodo. https://doi.org/10.5281/zenodo.8039833

Zhang, W. (2014). Estimate of lunar TiO_2 and FeO with M^3 data. *Encyclopedia of Lunar Science*, 1–7. https://doi.org/10.1007/978-3-319-05546-6_13-1

Zhang, X., & Cloutis, E. (2021a). Near-infrared spectra of lunar ferrous mineral mixtures. *Earth and Space Science*, *8*(4), e2020EA001153. https://doi.org/10.1029/2020EA001153

Zhang, X., & Cloutis, E. (2021b). Variations in the near-infrared spectral properties of ferrous mineral mixtures with different relative abundances. *Earth and Space Science*, *8*(9), e2021EA001636. https://doi.org/10.1029/2021EA001636

Zhang, X., Zhu, M. H., & Bugiolacchi, R. (2019). Mafic minerals in the South Pole-Aitken basin. *Journal of Geophysical Research: Planets*, *124*(6), 1581–1591. https://doi.org/10.1029/2018JE005870

Zhao, Z., Chen, J., Link, Z., Lu, X., & Li, Z. (2023). Chronology, composition, and mineralogy of mare basalts in the junction of Oceanus Procellarum, Mare Imbrium, Mare Insularum, and Mare Vaporum. *Icarus*, *397*, 115531. https://doi.org/10.1016/j.icarus.2023.115531

Zhu, M. H., Wunnemann, K., Potter, R. W. K., Kleine, T., & Morbidelli, A. (2019). Are the Moon's nearside-farside asymmetries the result of a giant impact? *Journal of Geophysical Research: Planets*, *124*(8), 2117–2140. https://doi.org/10.1029/2018JE005826